



Available online at www.sciencedirect.com

ScienceDirect

Comput. Methods Appl. Mech. Engrg. 417 (2023) 116393

Computer methods in applied mechanics and engineering

www.elsevier.com/locate/cma

Arbitrary curvature programming of thermo-active liquid crystal elastomer via topology optimization

Weichen Li^a, Xiaojia Shelly Zhang^{a,b,c,*}

^a Department of Civil and Environmental Engineering, University of Illinois Urbana-Champaign, 205 North Mathews Ave, Urbana, 61801, IL, USA

^b Department of Mechanical Science and Engineering, University of Illinois Urbana-Champaign, 1206 W. Green St., Urbana, 61801, IL, USA
^c National Center for Supercomputing Applications, 1205 W Clark Street, Urbana, 61801, IL, USA

Received 1 June 2023; received in revised form 27 July 2023; accepted 18 August 2023

Available online xxxx

Abstract

Plants can change their morphology upon environmental variations such as temperature. Inspired by plants' morphological adaptability, we present a computational inverse design framework for systematically creating optimized thermo-active liquid crystal elastomers (LCEs) that spontaneously morph into arbitrary programmed geometries upon temperature changes. The proposed framework is based on multiphysics topology optimization and a statistical mechanics-based LCE model to realize arbitrary curvature programming for LCE composites under large deformations. We propose a curvature-based optimization formulation that enables rotation-invariant and size-insensitive programmability of LCE, accounting for its highly nonlinear deformed shape. We demonstrate that the programmed LCE composites can accurately morph into a wide range of complex target shapes and curvatures, such as those of numbers, letters, flowers, and various objects. The resulting optimized designs exhibit highly irregular material distributions, which surpass intuition-based designs, and precisely produce desired deformed geometries upon temperature increase. The computational inverse design technique holds promise for a wide array of applications requiring function- and performance-driven design of active materials.

© 2023 Elsevier B.V. All rights reserved.

Keywords: Liquid crystal elastomer; Curvature programming; Spontaneous deformation; Inverse problem; Thermo-active materials; Multiphysics topology optimization

1. Introduction

Plants such as Rhododendron and Mimosa pudica exhibit morphological changes in response to environmental variations such as temperature and light [1,2] (Fig. 1A). Mimicking these behaviors, active materials such as hydrogel [3] and electroactive polymers [4] are manufactured for a wide range of engineering applications, and the programming of their active morphology changes have attracted great attention. In this study, we propose a multiphysics topology optimization framework to realize arbitrary shape-programming of a thermo-active soft material known as liquid crystal elastomer (LCE).

E-mail address: zhangxs@illinois.edu (X.S. Zhang).

^{*} Corresponding author at: Department of Civil and Environmental Engineering, University of Illinois Urbana-Champaign, 205 North Mathews Ave, Urbana, 61801, IL, USA.

LCE is a type of soft material that exhibits large and reversible spontaneous deformations under temperature stimuli [5–7]. This unique property makes LCE a strong candidate for environmentally responsive structures, such as temperature actuators [8], morphing structures [9], soft robotics [10,11], smart bio-medical devices [12], and artificial muscles [13,14]. Hence, the capacity to inversely program LCE's spontaneous deformation to achieve diverse prescribed behaviors would be highly valued.

The spontaneous deformation of nematic LCE is caused by the change of molecular orientation orders and can achieve a strain magnitude of over 50% [15]. As illustrated in Fig. 1B, LCE consists of rigid rod-like molecules known as mesogens bonded to a lightly crosslinked polymer network. At the nematic phase (low temperature), the mesogens exhibit a statistical orientation order with the average orientation known as the director n_0 . The rise in temperature increases the entropy of the molecules and weakens the orientation order. Beyond a transition temperature T_{cr} , the orientation order is completely lost, and the LCE becomes isotropic. The nematic-isotropic transition is manifested macroscopically as the spontaneous contraction along n_0 . The entropic nature of the response allows for the recovery of the original order and shape when the temperature decreases.

The types and magnitudes of LCE structures' spontaneous deformation are directly determined by the spatial distribution of the director. Different distributions produce distinct morphing patterns [5,6]. Therefore, the key to the applications of LCE is to inversely create the director distribution for targeted behaviors/functions [16]. In the literature, this is investigated using flat LCE sheets morphing out-of-plane where the spontaneous deformation is described by planar analytical models [17–19]. The shape of the morphed surfaces can be controlled through the parameters of the model [17,19] or by solving numerical inverse problems [18]. Complex surfaces, such as a human face [18], can be realized. Analytical approaches can also be applied to program the in-plane deformed shapes of LCE sheets [20], and include special features such as curved ridges and creases into the morphed surface by design [21–23]. Among these studies, the Gaussian curvature is frequently used to characterize the deformed surfaces as it is isometric invariant. Shape programming of LCE can also be realized directly through specialized fabrication techniques without analytical modeling or numerical computations, such as photo-curing the LCE members in pre-deformed states resembling the targeted shapes [24] and aligning the directors in principal curvature directions [25].

Besides analytical and fabrication-based methods, an alternative and promising approach to shape programming of LCE is topology optimization [26,27], as it has demonstrated great success in generating designs with optimized performance for a wide range of engineering disciplines, such as civil [28,29], aerospace [30], and bio-medical [31]. Topology optimization is increasingly accessible for new users thanks to many open-source codes [32]. The success prompts its use for designing structures with multiphysics and environmentally active behaviors, including magnetically responsive soft structure [33–35], piezoelectric composites [36,37], and materials with thermal-mechanical coupled behaviors [38,39]. For LCE composites, topology optimization is used to program the deformed shapes of origami folding of bi-layer LCE sheets [40] and the bending of LCE beams [41]. Both studies model LCE's spontaneous deformation as thermal expansion. Topology optimization is also used to generate designs of anisotropic active composites with minimized compliance under the small-deformation setup [42]. As LCE's spontaneous deformation is large fundamentally different from thermal expansion, accurate shape programming through topology optimization requires a rigorous and finite-deformation setup. However, such a method is underdeveloped, impeding full exploitation of LCE's actuation for realizing complex deformed shapes.

The development of a finite-deformation topology optimization framework for programming LCE's deformation must address three challenges. First, how to construct a systematic design characterization framework incorporating rigorous models for LCE's complex behaviors into the optimization. Second, how to realize efficient and stable numerical simulations of LCE's large and highly nonlinear deformation. Third, how to develop a robust optimization formulation that accurately captures the intrinsic features of the deformed shape.

Based on a rigorous LCE model and multiphysics topology optimization, this study develops a free-form inverse optimization framework for systematically programming the deformed shape of LCE composites to achieve any prescribed target shapes. The idea of this study is illustrated in Fig. 1C. Our main goal is to inversely optimize the spatial distribution and director orientation of LCE so that the composite can realize any prescribed shape in its temperature-induced deformed configuration as indicated in Fig. 1D. We adopt a continuum model of LCE developed based on the statistical mechanics of LCE's microstructures. The model accurately captures the temperature-induced anisotropic shape change and (semi-) soft elasticity of LCE. We then propose a characterization method based on multimaterial topology optimization that incorporates multiple candidate LCE directors as well

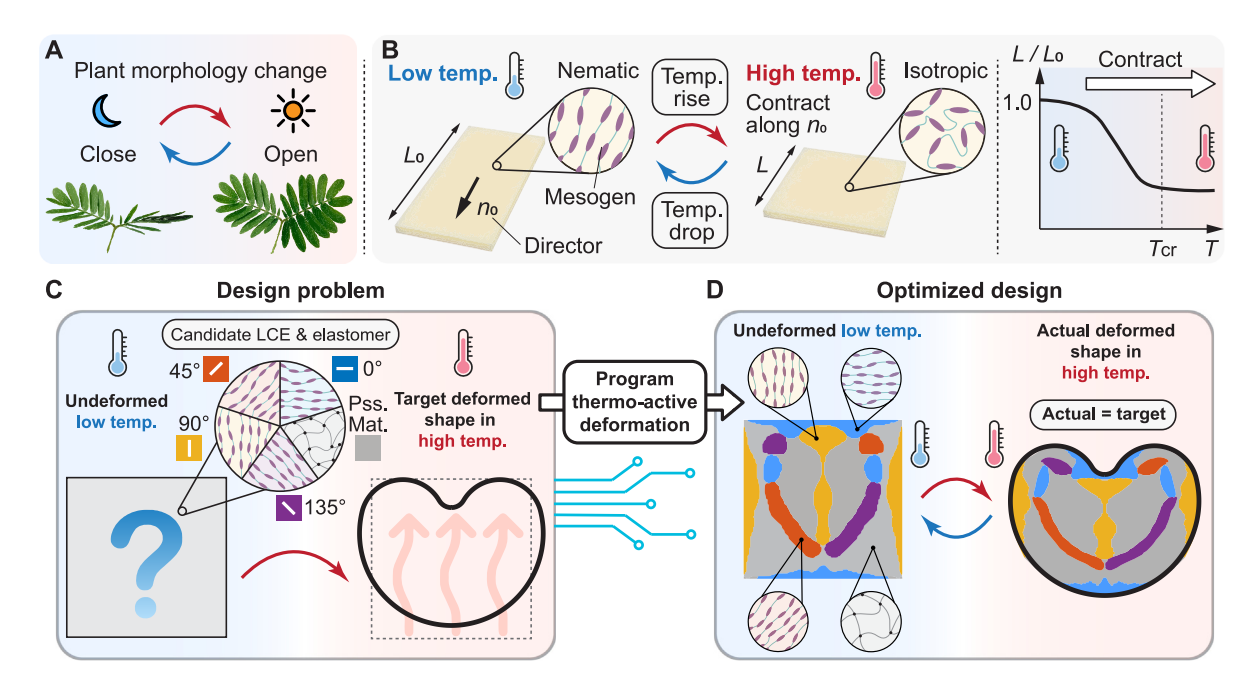


Fig. 1. Programming thermo-active behaviors of LCE composites. (A) Mimosa pudica changes its morphology based on light intensity; (B) mechanism of LCE's spontaneous temperature-induced deformation; (C) inverse optimization problem; (D) optimized design of LCE composite achieving prescribed deformed shape.

as a passive elastomeric material. Based on the characterization method, we develop the inverse optimization formulation for programming arbitrary deformed shapes of LCE. We propose a curvature-based description of the deformed shapes, which features several advantages critical for shape programming, such as rotation-invariant and size-insensitive. With the optimization framework, we inversely program LCE composites to achieve a wide range of complex prescribed target shapes, including those of numbers, letters, and objects such as an apple and a flower. The optimized designs show highly irregular distributions of LCE directors and accurately achieve the targets. Additionally, we also study optimized LCE actuators under temperature changes and reveal the unique benefits of a passive material phase in promoting actuation. The developed framework can benefit the design of a wide range of LCE-related active materials and structures.

The paper is organized as the following. Section 2 introduces the LCE model adopted in this study. Section 3 presents the proposed design characterization method, energy interpolation scheme, nonlinear finite element analysis, and the proposed inverse optimization formulation. Section 4 presents three groups of numerical examples with different targeted functions and dissimilar programmed behaviors. Section 5 provides some concluding remarks. Four appendices supplement the paper. Appendix A presents the derivation of semi-soft behavior predicted by the LCE model. Appendix B presents the design regularization and stabilization techniques for multimaterial finite-deformation topology optimization. Appendix C analyzes the error of the proposed curvature computation. Appendix D describes the post-processing of optimized designs.

2. Continuum model of LCE

This section introduces the continuum LCE model adopted by this study. The model is given in the form of a free-energy density function, which, with a fabrication-related condition, reduces to an anisotropic hyperelastic stored-energy density function with temperature dependence.

In some literature on the optimization of LCE, the spontaneous deformation of LCE is modeled as an anisotropic thermal expansion. Such an approach, however, may not capture the unique soft or semi-soft elasticity of LCE, which could lead to inaccurate estimates of macroscopic responses such as forces and displacements. This study adopts a rigorous model derived based on the statistical mechanics of LCE's microstructures, which accurately captures the spontaneous shape change and semi-soft elasticity of LCE.

2.1. Free-energy density for LCE

Rigorous modeling of LCE's behavior is pioneered by the neo-classical free energy density model [43–45]. The model is derived based on anisotropic Gaussian rubber considering the orientation order of mesogens. The free-energy density function of the neo-classical model is:

$$W_{NC}(\boldsymbol{F}, \boldsymbol{n}) = \frac{\mu}{2} \text{Tr}[\boldsymbol{l}_0 \boldsymbol{F}^T \boldsymbol{l}^{-1}(\boldsymbol{n}) \boldsymbol{F}], \qquad (1)$$

where $l_0 = a((1 - Q_0)\delta + 3Q_0n_0 \otimes n_0)$ and $l(n) = a((1 - Q)\delta + 3Qn \otimes n)$ are initial and current step length tensors that characterize anisotropy, and $Q_0, Q \in [0, 1]$ are initial and current order parameters that characterize the orientation order of the mesogens, respectively, and they are determined by the initial and current temperatures; n_0 and n are the initial and current director (unit vector), respectively; a is the step length of the freely-joint chain model; and δ is the Kronecker delta.

Its simple form encodes rich information about LCE behaviors, including spontaneous deformation, soft elasticity, director rotation, and coupled shear deformation when stretched perpendicular to the initial director [15], which can be observed in experiments and are absent in normal isotropic elastomers. The spontaneous deformation due to temperature change is realized through Q, which depends nonlinearly on the current temperature T.

The model (1), however, predicts a continuous zero-energy and zero-force soft mode [15,46,47], which disagrees with the soft behavior observed in the experiment; the latter exhibits an initial stiff phase for a small strain range followed by a long force plateau with small but non-zero stiffness, then finally ends with a third stiff phase with revived high stiffness [48,49]. Also, in the case of isotropic-to-nematic transition, the model predicts infinitely many director orientations. These issues would thwart numerical computation. A remedy is the improved semi-soft model that adds to (1) a non-ideal free energy to incorporate the nonideality due to non-uniform cross-linking [15,49]. The non-ideal model is expressed as [49]:

$$W_{NI}(\boldsymbol{F}, \boldsymbol{n}) = \frac{\mu}{2} \text{Tr}[\boldsymbol{l}_0 \boldsymbol{F}^T \boldsymbol{l}^{-1}(\boldsymbol{n}) \boldsymbol{F}] + \omega \frac{\mu}{2} \text{Tr}[(\boldsymbol{\delta} - \boldsymbol{n}_0 \otimes \boldsymbol{n}_0) \boldsymbol{F}^T \boldsymbol{n} \otimes \boldsymbol{n} \boldsymbol{F}], \qquad (2)$$

where ω is the non-ideality parameter. The W_{NI} term eliminates zero-stiffness soft modes and yields semi-soft responses with small but non-zero stiffness, which agrees with the experiment. The semi-soft stress-stretch curve predicted by (2) in the perpendicular stretch experiment shows the three-stage, stiff-soft-stiff feature. We note that there are more sophisticated models considering additional energy terms depending on the spatial gradient of n [15,50], i.e., ∇n , but those terms are of orders of magnitude smaller than the W_{NC} and W_{NI} and require element size in finite element analysis (FEA) to be smaller than a characteristic length at the order of 10 nm [15,50], which is impractical for the applications herein. Hence, the ∇n terms are not considered in this study. We note that model (2) (a variant) can accurately predict LCE's behavior not only in the uniaxial loading but also in the biaxial case [50]. Validation of the model in more complex stress states would be highly valuable and can be an interesting direction for future study.

In (2), both F and n are unknown and independent, indicating potential director rotation relative to the deformed matrix. The relative rotation (and overall LCE behaviors) is significantly influenced by the fabrication process [48] and crosslink densities [51]. LCE cross-linked in the nematic phase with relatively low temperature or high crosslink density shows limited relative director rotations and higher stiffness [48]. In this scenario, the director can be assumed "frozen" to the polymer matrix, and the current director n is determined by the macroscopic deformation F and the initial director n_0 through [51,52]

$$n = \frac{F n_0}{|F n_0|} \tag{3}$$

The condition (3) removes the independence of n and specializes (2) to the following anisotropic stored-energy density function:

$$W_{FZ}(\mathbf{F}) = \frac{\mu}{2} \left[\frac{1 - Q_0}{1 - Q} \operatorname{Tr}(\mathbf{C}) + \left(\frac{3Q_0}{1 + 2Q} - \omega \right) \mathbf{n}_0 \cdot \mathbf{C} \mathbf{n}_0 - \left(\frac{3Q(1 - Q_0)}{(1 - Q)(1 + 2Q)} - \omega \right) \frac{\mathbf{n}_0 \cdot \mathbf{C}^2 \mathbf{n}_0}{\mathbf{n}_0 \cdot \mathbf{C} \mathbf{n}_0} \right], \tag{4}$$

where $C := F^T F$ is the right Cauchy-Green deformation tensor. The model's (4) sole dependence on F considerably reduces computational cost compared to (2).

We note that nematic genesis needed for the frozen-director condition may not always be preferable for fabrication. For LCE with isotropic genesis where the director can freely rotate, the frozen-director condition could be inappropriate and should be removed, which recovers (4) to (2). In that case, the displacement and director fields are independent and are determined through energy minimization. In addition, a Lagrange multiplier field for the inextensibility constraint of n needs to be solved. Hence, lifting the frozen director condition would increase the computational cost.

The models (1), (2), and (4) are Gaussian or Gaussian-based, and they are appropriate for entropy-dominated LCEs. For modeling LCE with more general types of nonlinearity, non-Gaussian models such as the Ogden-type extension proposed in [53] are available. Also, LCE is essentially viscoelastic [54], and accurately modeling its non-steady and rate-dependent responses such as hysteresis requires a viscoelastic model (e.g., [55]).

2.2. Two-stage semi-soft elasticity: the perpendicular stretch experiment

One of the unique features of LCE is that it exhibits (semi-)soft behavior, which can be revealed experimentally through applying stretch perpendicular to the initial director n_0 in an isothermal condition [15] as indicated in Fig. 2A. When the LCE sample is stretched, the director remains initially static, but after a critical stretch, the director starts to rotate and coupled shear deformation occurs to achieve a lower energy state. Accompanying the director rotation and shear is the sudden drop of stiffness in the stress–stretch curve, resulting in the soft behavior. When stretched further, depending on how the LCE is made and whether it is modeled with the frozen-director condition, LCE could establish a third stage with revived high stiffness [15,48,49].

Here, we demonstrate that the frozen-director model (4) can predict a two-stage semi-soft behavior, which cannot be captured by standard hyperelastic models used in some studies to model LCE. We analytically study the model (4) with $\mu=2$ and $\omega=0.1$ (chosen for better illustration and only for this theoretical analysis, not for the material parameters used in the examples) and a deformation gradient F chosen to represent the kinematics of the stretch experiment. The obtained analytical relations of stress, lateral stretch, director orientation, and coupled shear deformation as a function of the applied stretch are plotted in Figs. 2B to E, respectively. It can be seen that in Stage I, LCE behaves in a standard uniaxial fashion with no director rotation and shear. When the applied stretch enters Stage II, stiffness drops significantly, and stretch in out-of-plane direction (λ_{zz}) freezes while vertical stretch λ_{yy} accelerates its descent. Meanwhile, the director starts to rotate and asymptotically converges to $\pi/2$ when stretch approaches infinity, and coupled shear also occurs with a speed initially fast and subsequently decaying. Macroscopically, the shear deformation appears in a zig-zag and alternating fashion in the vertical direction, forming the "stripe pattern" observed in experiments [56]. For the derivation of the analytical relations in Fig. 2, the readers are referred to Appendix A. We note that the model without the frozen director condition (2), which suits LCE fabricated in the isotropic phase, predicts a three-stage, stiff-soft-stiff stress-stretch response. The three-stage response is widely studied analytically and experimentally. For more details, the readers are referred to [15,49].

In this study, the values of the LCE parameters are chosen as $Q_0 = 0.5$, $\mu = 0.0829$, and $\omega = 0.0401$ based on experimental results in the literature. The Q_0 value is a typical value for the nematic-phase LCE as shown in [57,58]. The value of μ is chosen to match the 0.04 MPa initial slope of the stress–strain curve obtained in the direction perpendicular to the director of a nematic-genesis LCE sample in [48] (sample 7 g of the study). The value of ω is chosen to match the 0.027 MPa critical stress (corresponding to the kink of the stress–strain curve) of the same test result in [48].

2.3. Temperature-induced, stress-free spontaneous deformation

The stress-free, spontaneous deformation along the n_0 can be obtained by taking the stationary condition of (4), which leads to:

$$\lambda_{\text{spon}}(Q) = \left[\frac{(1 - Q_0)(1 + 2Q)}{(1 - Q)(1 + 2Q_0)} \right]^{\frac{1}{3}}.$$
 (5)

This expression is the same with or without the frozen-director condition as the stress-free contraction or extension aligns with n_0 and preserves $n = n_0$. It can be seen that λ_{spon} depends solely and nonlinearly on Q_0 and Q. Based on (5), a nematic-isotropic transition ($Q_0 = 0.5$ and Q = 0) produces a spontaneous contraction (stretch) of 0.63,

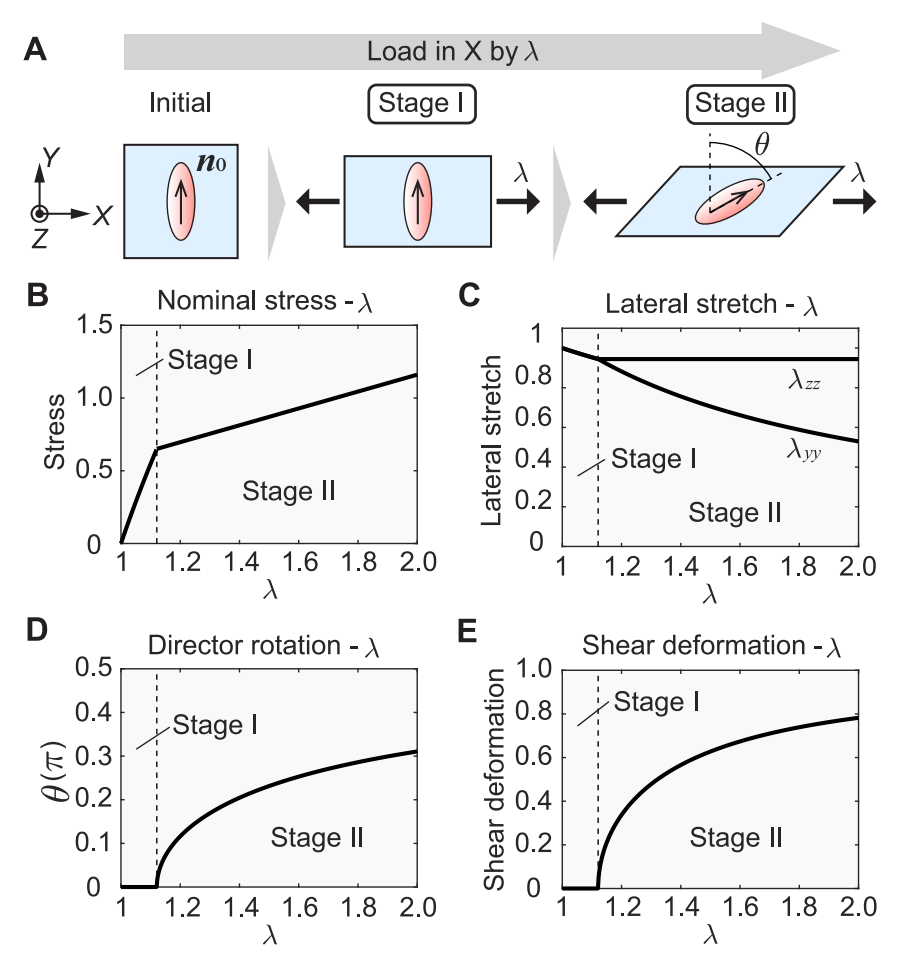


Fig. 2. Semi-soft elasticity predicted by the frozen-director model W_{FZ} . (A) The stretch experiment with applied axial stretch perpendicular to n_0 ; (B) nominal stress-stretch relation; (C) lateral deformation-stretch relation; (D) director rotation-stretch relation; (E) shear deformation-stretch relation.

and an isotropic-nematic transition produces a spontaneous extension of 1.6. The magnitude of both values agrees with experimental observations [15]. The order parameters Q_0 and Q depend on the initial and current temperatures, i.e., T_0 and T, respectively. The Q-T relation is in general nonlinear and monotonically decreasing with Q reaching 0 (isotropic state) at the transitional temperature T_{cr} [15]. While the shape of the Q-T curve is similar for different nematic LCEs, the value of T_{cr} depends heavily on the LCE material composition and fabrication process. The T_{cr} of different LCEs can vary from 20 °C [59] to over 120 °C [60]. As this study is not restricted to a specific type of LCE and requires no direct temperature information for numerical simulation, we do not assume a specific Q-T relation but instead directly load the LCE composite through Q in FEA. If the application scenario requires a Q-T relation, one can adopt established models such as the power law in [61,62].

2.4. Plane stress condition

As this study focuses on 2D LCE composite structures with in-plane n_0 and identical material distribution in the thickness direction, we assume the plane stress condition and absence of out-of-plane warping. Computation-wise, the plane stress condition enables standard displacement-based 2D FEA with incompressible materials. With the X and Y axes lying in the plane, the plane stress condition requires $F_{13} = F_{23} = F_{31} = F_{32} = 0$ [63], and other

components are, in general, none-zero. In the context of LCE, such F implies that any stripe pattern would take place in-plane rather than through the thickness direction. With this form of F and $n_{0,3}=0$ (n_0 in-plane), by substitution, we obtain the 2D plane-stress version of W in (4) in terms of the 2D deformation gradient \overline{F} and 2D director \overline{n}_0 as:

$$W(\overline{F}) = \frac{\mu}{2} \left[\frac{1 - Q_0}{1 - Q} \left(\text{Tr}(\overline{C}) + \frac{1}{\overline{f}^2} \right) + \left(\frac{3Q_0}{1 + 2Q} - \omega \right) \overline{\boldsymbol{n}}_0 \cdot \overline{\boldsymbol{C}} \overline{\boldsymbol{n}}_0 - \left(\frac{3Q(1 - Q_0)}{(1 - Q)(1 + 2Q)} - \omega \right) \frac{\overline{\boldsymbol{n}}_0 \cdot \overline{\boldsymbol{C}}^2 \overline{\boldsymbol{n}}_0}{\overline{\boldsymbol{n}}_0 \cdot \overline{\boldsymbol{C}} \overline{\boldsymbol{n}}_0} \right], \tag{6}$$

where $\overline{C} := \overline{F}^T \overline{F}$, and $\overline{J} := \det(\overline{F})$. Notice that the form of the 2D energy (6) is similar to the 3D version (4), except for the appearance of \overline{J} in the 2D version. This term is from $\operatorname{Tr}(C)$ term in (4) and implies planar stretchability although the material is incompressible. The 2D model (6) is used for finite element implementation.

In addition to LCE, we also include isotropic hyperelastic materials inactive to temperature as candidate materials for optimization. The material is referred to as the passive material throughout this paper. Its behavior is described by the neo-Hookean model, with the 2D plane-stress stored energy density function $W_P(\overline{F}) = \frac{\mu_P}{2} \left(\text{Tr}(\overline{C}) + (\overline{J})^{-2} - 3 \right)$ where μ_P is the shear modulus of the passive material.

For applications involving three-dimensional stress states and deformations, such as 3D LCE structures and 2D LCE sheets with out-of-plane bending, the general 3D model (4) or (2) should be adopted. This would, however, lead to increased computational cost caused by not only the curse of dimensionality but also solving for the Lagrange multipliers associated with incompressibility and, for the free-director case (2), inextensibility of n.

3. Optimization formulation for programming arbitrary deformed shape of LCE

3.1. Multimaterial characterization of LCE composites

In this study, we aim to optimize the geometry of LCE material and its director distribution to achieve prescribed deformed shapes or maximized actuation upon temperature change. This requires a systematic design characterization of LCE composites consisting of LCEs with different candidate directors and a passive, isotropic elastomer. We employ a multimaterial characterization approach used in topology optimization to represent multiple anisotropic materials, such as fiber-reinforced elastomers [64] and soft materials with magnetization directions [33].

3.1.1. Characterization of structural geometry

The geometry of the LCE composite is characterized by a density design variable ρ with ρ_e associated with element e. The value of $\rho_e = 1$ indicates that the domain of element e is solid, and $\rho_e = 0$ means that the domain is void (no material). To achieve mesh independence, minimal size regularization, and near-discreteness of the design variables, we apply the standard filter technique [65] and Heaviside projection [66] to obtain the physical variable $\overline{\rho}_e$, which is used to represent the physical geometry of the LCE composites. Details of the filter and projection are provided in Appendix B.

3.1.2. Characterization of material phases

In this study, LCE with different directors n_0 and passive material are characterized as different material phases for the optimization, which allows the use of established multimaterial characterization frameworks. This study adopts the Hypercube-to-Simplex Projection (HSP) approach [67], which has been used in multimaterial topology optimization [33,64].

The HSP approach relates a set of material design variables ξ with the physical material variable m used to represent the material phase distribution of the LCE composite. Assuming a total of M+1 material phases (M phases of LCE with different directors plus a passive material), the physical variable is m is a $N \times (M+1)$ matrix with $m_e^{(j)}$ denoting the (e, j) component and representing the proportion of material phase j in element e; and the material design variable ξ is a $N \times M$ matrix. Based on the HSP, the relation mapping of ξ to m is

$$\overline{m}_e^{(j)} = \sum_{i=1}^{2^M} s_i^{(j)} \left((-1)^{\left(M + \sum_{k=1}^M c_i^{(k)} \right)} \prod_{l=1}^M \left(\overline{\xi}_e^{(l)} + c_i^{(l)} - 1 \right) \right), j = 1, \dots, M,$$

$$(7)$$

and $\overline{m}_e^{(M+1)} := 1 - \sum_{j=1}^M \overline{m}_e^{(j)}$, where $c_i^{(j)}$ is the *i*th vertex of a *M*-dimensional unit hypercube for the *j*th material phase, and $s_i^{(j)}$ is the mapped vertex of a *M* dimensional standard simplex domain:

$$s_i^{(j)} = \begin{cases} \frac{c_i^{(j)}}{\sum_{q=1}^M c_i^{(q)}} & \text{if } \sum_{q=1}^M c_i^{(q)} \ge 1\\ 0 & \text{otherwise,} \end{cases}$$
 (8)

and $\overline{\xi}_e^{(l)}$ is the projected material variable obtained through the same filtering and projection procedure as $\overline{\rho}_e$. We note that $\overline{m}_e^{(j)} \geq 0, j = 1, \dots, M$ and $\sum_{j=1}^M \overline{m}_e^{(j)} \leq 1$.

The two physical variables $\overline{\rho}$ and \overline{m} can fully represent the geometry and material distribution of any composites with M LCE directors and a passive material phase up to the finite element resolution.

3.2. Interpolation of stored-energy density function

Continuous optimization requires interpolation of material properties (i.e., stored energy density functions) based on the physical variables. Based on the HSP approach, the fictitious mixed material's energy inside element e is interpolated through the physical variables as

$$W_{e}(\overline{F}; \overline{\rho}_{e}, \overline{m}_{e}, \gamma_{e}) := [\epsilon + (1 - \epsilon)\overline{\rho}_{e}^{p}] \sum_{i=1}^{M+1} (m_{e}^{(j)})^{p_{\xi}} \tilde{W}^{(j)}(\overline{F}; \gamma_{e}),$$

$$(9)$$

where $\epsilon=10^{-6}$ is a small number to prevent singularity, p and p_{ξ} are penalization parameters, and $\gamma_e\in[0,1]$ is a near-discrete dependent variable of $\overline{\rho}_e$ serving as the characteristic field such that $\gamma_e=1$ in solid regions and $\gamma_e=0$ in void regions. Its expression is given in Appendix B. The $\tilde{W}(\overline{F};\gamma_e)$ is given as [68,69]:

$$\widetilde{W}^{(j)}(\overline{F}; \gamma_e) := W^{(j)}(\gamma_e \overline{F}) - W_{PL}(\gamma_e \overline{F}) + W_{PL}(\overline{F}), \tag{10}$$

where, if $j \leq M-1$, $W^{(j)}(\overline{F})$ is the (plane stress) LCE energy density given in (6) with j denoting the jth candidate director $\mathbf{n}_0^{(j)}$, and if j = M, $W^{(M)}(\overline{F})$ is the neo-Hookean energy density representing the passive material; $W_{PL}(\overline{F}) := \frac{1}{2}\overline{\varepsilon}(\overline{F}) : \overline{\mathbb{C}_0} : \overline{\varepsilon}(\overline{F})$ being the linearized plane-stress stored-energy function for the void regions used to prevent numerical instability [68,69], and $\overline{\mathbb{C}_0}$ is the plane-stress isotropic incompressible elastic tensor for the passive void-region fictitious material defined by the corresponding shear modulus μ_0 . Here, we take $\mu_0 = \min\{\mu, \mu_P\}$.

The introduction of γ and W_{PL} is for preventing numerical instability in void regions, which is a common numerical issue in large-deformation topology optimization if no special treatments are applied [68]. We note that, in solid regions ($\overline{\rho}_e = 1$ and $\gamma_e = 1$), the interpolated energy (9) recovers the LCE model (6) (if $j \leq M$) or the passive material model W_P (if j = M + 1), and both are physically well-defined. In void regions ($\overline{\rho}_e = 0$ and $\gamma_e = 0$), the stored energy (9) becomes $\epsilon W_{LP}(\overline{F})$, which is orders of magnitudes smaller than the energy in the solid region such that its influence on the global behavior of solid regions is negligible [69].

3.3. Nonlinear FEA for LCE composites

We use the finite element method (FEM) to solve the elastostatics problem of LCE under temperature change realized by $Q \neq Q_0$. We adopt the standard displacement-based 2D FEM with the total Lagrangian formulation and quadrilateral bilinear element with four Gauss points. In the FE discretized domain, the global displacement vector at the equilibrium \mathbf{u} of the LCE composite defined by $\boldsymbol{\rho}$ and $\boldsymbol{\xi}$ is obtained by minimizing the total potential energy $\Pi(\boldsymbol{\rho}, \boldsymbol{\xi}, \boldsymbol{v})$ with respect to the global FE displacement vector \boldsymbol{v} , i.e.,

$$\boldsymbol{u}(\boldsymbol{\rho}, \boldsymbol{\xi}) = \arg\min_{\boldsymbol{v} \in K} \Pi(\boldsymbol{\rho}, \boldsymbol{\xi}, \boldsymbol{v}) := \sum_{e} \int_{\Omega_{0,e}} W_{e}\left(\overline{\boldsymbol{F}}(\boldsymbol{v}_{e}); \overline{\rho}_{e}(\boldsymbol{\rho}), \overline{\boldsymbol{m}}_{e}(\boldsymbol{\xi}), \gamma_{e}(\boldsymbol{\rho})\right) d\Omega, \tag{11}$$

where K is the kinematically admissible set, $\Omega_{0,e}$ is the domain of element e in the reference configuration, \mathbf{v}_e is the 2D element displacement vector, and W_e is given in (9). The stationary condition requires:

$$r(\rho, \xi, v) := \frac{\partial \Pi(\rho, \xi, v)}{\partial v} = \mathbf{0}.$$
 (12)

The nonlinear equation (12) is solved by the Newton-Raphson method where the tangential stiffness matrix at displacement v is $\mathbf{K}(\rho, \xi, v) := \partial^2 \Pi(\rho, \xi, v)/\partial v^2$. For more details about nonlinear FEA, the readers are referred to [63].

3.4. Optimization formulation

Here, we first present the optimization formulation with a general objective function for the inverse optimization of LCE composites. In the following subsection, we will introduce and elaborate on the specific form of the objective function, which is the proposed curvature-based description. The inverse optimization problem can be stated as: vary the density and material design variables (and potentially additional design variables) to minimize an objective function subject to certain constraints. Mathematically, it is stated as:

$$\min_{\boldsymbol{\rho},\boldsymbol{\xi},z} J\left(\boldsymbol{\rho},\boldsymbol{\xi},z,\boldsymbol{u}(\boldsymbol{\rho},\boldsymbol{\xi})\right) + \alpha V(\boldsymbol{\rho}) + \alpha_{LCE} V_{LCE}(\boldsymbol{\rho},\boldsymbol{\xi})$$
s.t. $V(\boldsymbol{\rho}) - V_0 \le 0$

$$\rho_e, \xi_e^{(j)} \in [0,1] \qquad e = 1, \dots, n; \quad j = 1, \dots, M$$
with $\boldsymbol{u}(\boldsymbol{\rho},\boldsymbol{\xi})$ such that $\boldsymbol{r}\left(\boldsymbol{\rho},\boldsymbol{\xi},\boldsymbol{u}\right) = \boldsymbol{0}$.

where J is the part of the objective function used to describe the targeted performance of the LCE composite (such as the error between the actual and target deformed shapes), and its specific form will be given in the following subsections, z stands for additional and optional design variables. We include two volume penalization terms in the objective function to (mildly) penalize the total volume V and total LCE volume V_{LCE} for removing possible superfluous materials in the final design. The total volume is also set as a constraint that specifies the maximum allowable total volume fraction V_0 in the design. The constraint can be seen as removed if $V_0 \ge 1$. Finally, the (discretized) nonlinear state equation is satisfied by requiring the residual r = 0.

The sensitivity of the objective and constraint functions with respect to the design variables are obtained with the adjoint method through:

$$\frac{\partial \phi}{\partial y_e} = \frac{\partial \phi \left(\boldsymbol{\rho}, \boldsymbol{\xi}, \overline{\boldsymbol{u}} \right)}{\partial y_e} \bigg|_{\overline{\boldsymbol{u}}} + \boldsymbol{\lambda}^{\mathrm{T}} \frac{\partial \boldsymbol{r} \left(\boldsymbol{\rho}, \boldsymbol{\xi}, \overline{\boldsymbol{u}} \right)}{\partial y_e} , \tag{14}$$

where ϕ is either the objective or constraint function, y_e is either ρ_e or ξ_e , and λ is the adjoint vector attained by solving the adjoint system:

$$K^{\mathrm{T}}(\rho, \xi, \overline{u}) \lambda = -\frac{\partial \phi(\rho, \xi, \overline{u})}{\partial \overline{u}}.$$
(15)

The sensitivity is input to the gradient-based method of moving asymptotes (MMA) [70] to update the design iteratively.

3.5. Curvature-based formulation for programming the deformed shapes of LCE composites

The inverse optimization requires defining a variable capable of robustly and accurately characterizing the deformed shape of LCE composites, and this is challenging for three reasons. First, the variable should accurately represent the inherent properties of the geometry and be independent of overall orientation or observer change. Second, the variable should be unrelated or insensitive to overall scaling so that a shape with different sizes should be characterized as the same kind. Third, the variable should be based on the current deformed configuration which, in general, differs significantly from the undeformed configuration in shape, area, and length. These requirements rule out the straightforward location-based formulation that assigns target locations to a collection of material control points, as such a formulation is defined with respect to an overall orientation and absolute size, hence being too restrictive for optimization. Also, any intuitively determined target locations are unlikely to be those that are most easily achievable by the LCE composites, hence deteriorating the accuracy of the programmed shape.

To address the above challenges, we propose a curvature-based characterization for programming the deformed shape of LCE composites as illustrated in Fig. 3A. The main idea is that we program the curvature of a curve describing the current deformed configuration of the composite to match prescribed target values. As illustrated in the optimization setup of Fig. 3A, the formulation is built upon a collection of material control points that form a

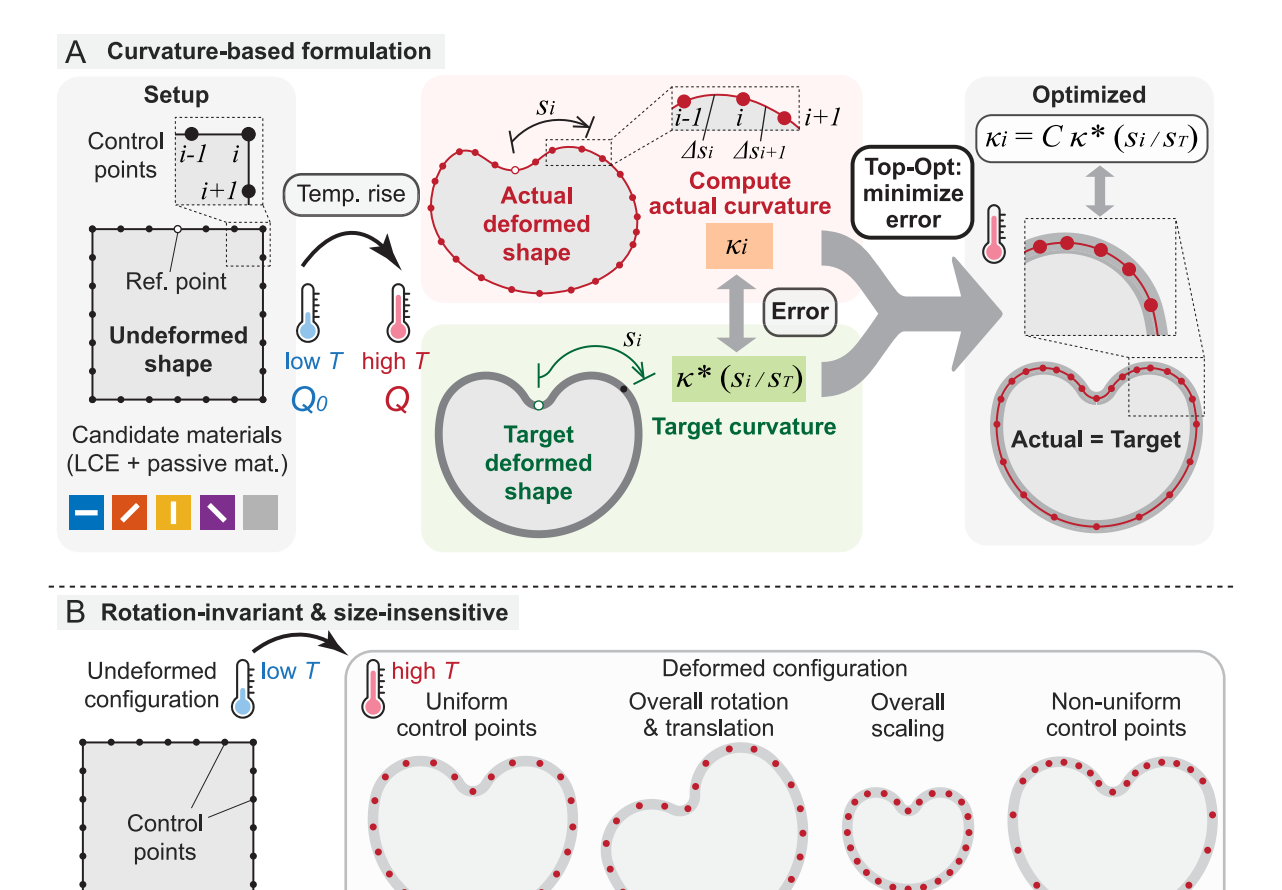


Fig. 3. Proposed inverse optimization formulation. (A) Illustration of the curvature-based formulation: the error between the actual and target curvatures is minimized to realize the target shape; (B) different control point realizations of the same target shape.

Different realizations of the same target

discretized curve. Upon temperature rise, the LCE composite and the curve deform to their current configurations. Then, the (discretized) curvature of the current curve κ is programmed to match the specified target curvature (κ *) through topology optimization. When the error between the actual and target curvatures is minimized, the actual deformed shape will match the target. Accordingly, the objective function to be minimized is defined as the error between the actual and target curvatures, i.e.,

$$J(\boldsymbol{\rho}, \boldsymbol{\xi}, C, \boldsymbol{u}(\boldsymbol{\rho}, \boldsymbol{\xi})) = \frac{1}{2N} \sum_{i=1}^{N} \left[\kappa_{i} \left(\boldsymbol{u}(\boldsymbol{\rho}, \boldsymbol{\xi}) \right) - C \kappa^{*} \left(\frac{s_{i} \left(\boldsymbol{u}(\boldsymbol{\rho}, \boldsymbol{\xi}) \right)}{s_{T} \left(\boldsymbol{u}(\boldsymbol{\rho}, \boldsymbol{\xi}) \right)} \right) \right]^{2}, \tag{16}$$

where N is the total number of material control points, κ_i is the (discretized) curvature of the ith control point, κ^* is the prescribed target curvature function that depends on the normalized arc length of the control point, with s_i being the arc length of the ith control point measure from a reference control point and s_T the total arc length, and scalar C is a dummy design variable for removing size dependence.

As illustrated in Fig. 3B, the proposed curvature formulation is independent of overall rotations and translations of the deformed configuration. The formulation is also insensitive to overall scaling due to the introduction of the dummy design variable C as the optimizer can choose any (positive) C value to scale the target curvature for achieving a better fit. Finally, the formulation is insensitive to the distribution of the control points in the current configuration, as the target curvature κ^* is formulated as a function that depends on the control point's

relative location s_i/s_T along the curve. For a control point, a change of location (e.g., at different optimization steps) indicates a change of its κ^* value, which is determined based on the spatial description of the target shape. Conceptually, such treatment of κ^* implies two mechanisms for the optimizer to improve fitting. The first is to change κ_i without changing the location s_i/s_T and κ^* , and the second is to change κ^* through changing the location s_i/s_T but without altering κ_i . The second mechanism automatically deactivates when the target curvature is constant (e.g., a circular or linear segment). We note that κ^* should not be formulated as pre-determined and fixed values for the control points as the target value depends on the current locations that are generally unknown before solving the state equations. As illustrated in Fig. 3B, the formulation can effectively consider the three different types (and their combinations) of realizations of the same target shape, and hence, it enjoys a large optimization search space unavailable for location-based and size-sensitive formulations.

For the computation of κ_i in (16), the continuous formula is $\kappa(s) = x'(s)y''(s) - y'(s)x''(s)$ where s is the current arc length, and x and y are the current planar locations at s with the prime denoting derivatives with respect to s. Based on this formula, we use a three-point finite difference scheme to compute the discretized curvature κ_i , i.e.,

$$\kappa_{i} = \frac{x_{i+1} - x_{i-1}}{\Delta s_{i} + \Delta s_{i+1}} \frac{4(y_{i+1} - 2y_{i} + y_{i-1})}{(\Delta s_{i} + \Delta s_{i+1})^{2}} - \frac{y_{i+1} - y_{i-1}}{\Delta s_{i} + \Delta s_{i+1}} \frac{4(x_{i+1} - 2x_{i} + x_{i-1})}{(\Delta s_{i} + \Delta s_{i+1})^{2}},$$
(17)

where $\Delta s_i := s_i - s_{i-1}$ as indicated in the top middle box of Fig. 3A. Note that the distance of control points in the current configuration is generally non-uniform even if they are uniform in the undeformed configuration. Hence, the standard three-point central difference in (17) is not second-order accurate as it is in the equidistant case. However, our numerical investigations show satisfactory fitting of the target shape. An error analysis of the curvature computation (17) is provided in Appendix C. The first set of examples will also discuss the influence of the error.

4. Results

This section demonstrates the effectiveness of the proposed framework and curvature formulation in achieving various target shapes with different complexities. In addition to programming LCE's deformed shape, we also investigate maximizing the actuation displacement of LCE composites, as LCE is frequently used as actuators.

For the curvature programming, we focus on optimizing the material distribution through ξ and not the structural topology represented by ρ , and the latter is frozen to 1. To avoid bad local optima, we adopt a continuation scheme for the penalization parameter p_{ξ} and Heaviside parameter β_{ξ} , both are initially set to 1. At the 100th step, p_{ξ} starts to increase by 0.5 every 20 steps until reaching 3 at the 180th step, where β_{ξ} starts to increase with the same pattern and reaches 64 at the 300th step. The maximum number of steps is set to 330. Although the Heaviside projection is employed, small regions with mildly mixed materials can still appear in some design cases. To ensure the complete discreteness of the final design, we apply a discrete projection as post-processing to the optimized results. Details of the discrete projection are provided in Appendix D. The responses presented in this paper are those of the discrete designs.

4.1. Strip morphing into complex shapes

In this subsection, we aim to program the deformed shape of a slender and solid (no voids) LCE composite strip as indicated in Fig. 4A. The strip domain has a size of $L \times H = 400 \text{ mm} \times 8 \text{ mm}$ (with 1-mm thickness) and is fixed on the left edge. The FE mesh for the domain is 400×8 . We consider two material phases (M=1): LCE with n_0 along the longitudinal direction and a passive neo-Hookean elastomer. This is because the strip deforms mainly in bending which can be actuated by LCE contraction on the top or bottom layer of the strip. As will be shown in the results, considering only one LCE director candidate is sufficient for the accurate realization of various shapes. Also, as will be demonstrated later that the strip structure deforms mainly in bending and shows little axial deformation because of its slender geometry, we assume unchanged arc lengths before and after the deformation only for this example in Section 4.1. The constant arc length assumption simplifies the computation of the current curvature expression from (17) to $\kappa_i = \left(\frac{x_{i+1}-x_{i-1}}{2\Delta S}\right)\left(\frac{y_{i+1}-2y_i+y_{i-1}}{(\Delta S)^2}\right)-\left(\frac{y_{i+1}-y_{i-1}}{2\Delta S}\right)\left(\frac{x_{i+1}-2x_i+x_{i-1}}{(\Delta S)^2}\right)$ where ΔS is the (equidistant) segment length between the material control points as indicated in 4A. The simplification also allows for prescribing a fixed target curvature value to each material point, i.e., the κ^* in (16) reduces to a scalar constant from a function. The constant arc length assumption is not applied to examples in Sections 4.2 and 4.3.

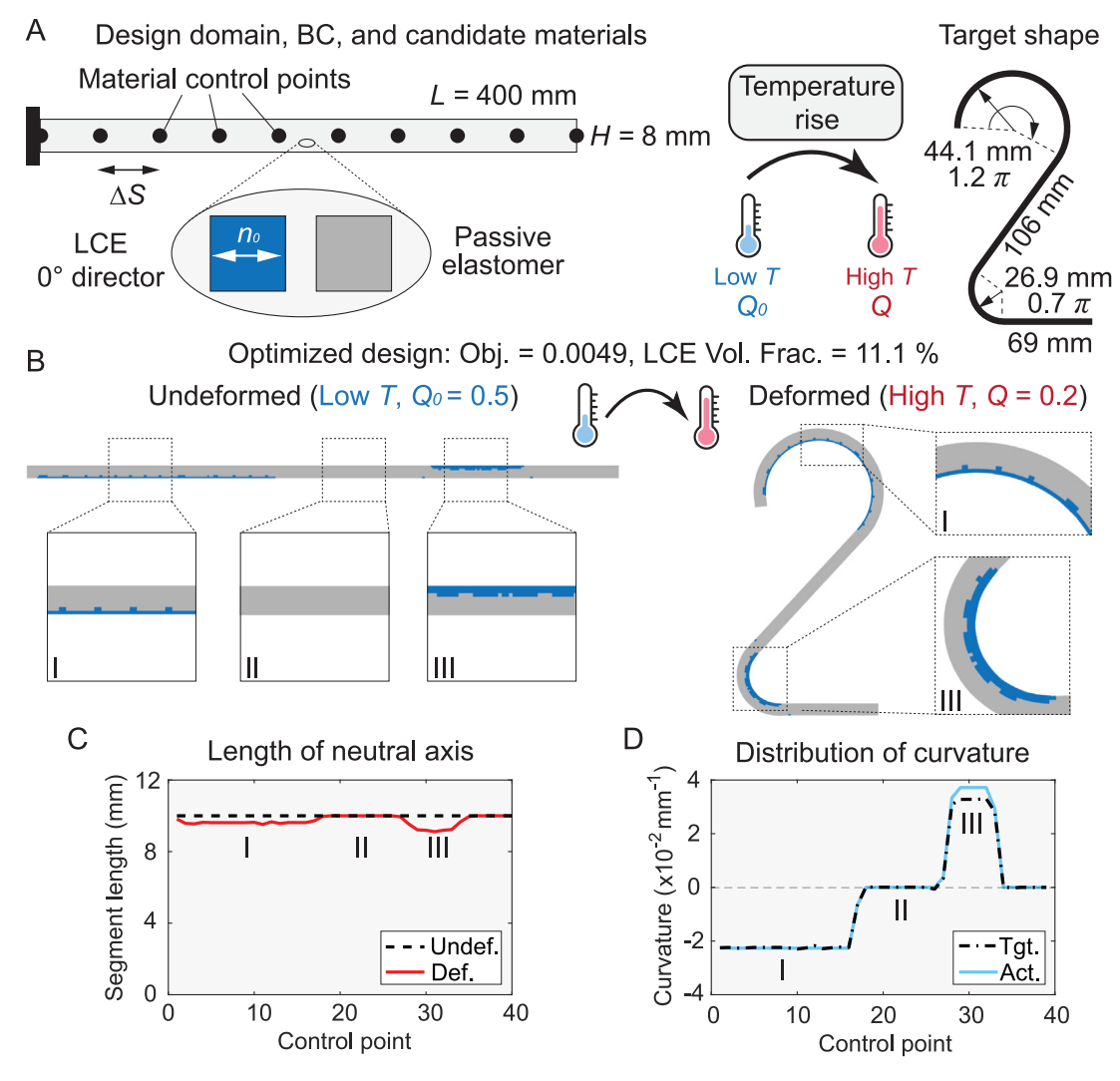


Fig. 4. Inverse optimization of a strip LCE composite realizing the shape of number 2. (A) Optimization setup; (B) optimized design in undeformed and deformed configurations; (C) distributions of undeformed and deformed neutral axis length segments; (D) distributions of target and actual curvatures. (For interpretation of the references to color in this figure legend, the reader is referred to the web version of this article.)

As we focus on solid LCE composite strips, only the material variable ξ is optimized, and the density variable $\rho=1$ is excluded from the optimization. We use a total of N=39 control points that equally divide the neutral axis into 40 segments as illustrated in Fig. 4A. Other parameters are set as follows: $\alpha_{LCE}=0.05$, $V_{LCE,0}=1$, and the filter radius is 3 mm. With this setup, we aim to program the strips into target shapes of numbers 2, 3, 6, and 7, which have varying curvatures along their arc lengths. These target shapes are represented by tangentially joined circular and linear segments with total arc lengths equal to the length of the domain, i.e., 400 mm. Hence, for any region of a target shape, the target curvature is either a constant or zero. The computer configuration is CPU: AMD Ryzen Threadripper 3970X 32-Core Processor 3.69 GHz and RAM: 256 GB. For this family of examples, the average computational time for the entire optimization process (with maximum 330 optimization steps) is approximately 45 min.

We first focus on the target shape of number 2 as indicated in Fig. 4A and use Q=0.2 (before reaching the isotropic state). The target shape comprises two circular arcs and two line segments joining tangentially. Starting from the top left of the number 2, the first arc has a radius of 44.1 mm and an angle of 1.2π , and the first line segment

has a length of 106 mm, then the second arc has a radius of 26.9 mm and an angle of 0.7π , and finally, the second line segment has a length of 69 mm. The corresponding optimized designs (undeformed and deformed) are shown in Fig. 4B, with blue indicating the LCE and gray indicating the passive elastomer. For illustration, the deformed shape is rotated to align with the normal orientation of the number 2, which will not alter the curvature and hence the objective function. The deformed configuration shows the accurate realization of the shape of the number 2. As expected, the distribution of LCE concentrates on the sides of the strip to effectively generate curvature through the temperature-induced axial contraction as demonstrated in Fig. 4B. The volume of LCE is about 11.1% of the strip, indicating that complex shapes can be realized with a relatively small amount of LCE. As a check for the constant arc length assumption, Fig. 4C shows the actual deformed arc length segments among the control points versus the undeformed values. The deformed arc length remains largely unchanged from the initial ones, which justifies the constant arc length assumption. Some mild changes are seen in Parts I and III of the strip where LCE appear. Fig. 4D shows the distribution of the actual and target curvature along the neutral axis, which verifies the overall accurate fitting. Small discrepancies appear in Part III due to post-processing that removes some mildly mixed materials (LCE and passive material) on the convex side of the deformed strip, leading to the locally magnified curvature.

Using the inverse optimization framework, we can achieve the same target shapes under a wide range of temperatures (Q values). This is demonstrated in Fig. 5A, where the results are obtained with Q=0,0.1,0.2, and 0.3, respectively. As shown in the deformed configurations, the results with Q=0,0.1, and 0.2 achieve the target shape of 2 fairly accurately, but Q=0.3 produce a poor fit due to insufficient actuation. This trend is quantitatively shown in the objective function value-Q plots in Fig. 5A. Also, larger Q (lower current temperatures) requires more LCE to generate the target curvatures as shown in the nonlinear Q-LCE volume fraction curve in Fig. 5A.

Change in the passive material stiffness alters the final LCE volume while retaining accurate fits as demonstrated in Fig. 5B, which shows the objective function value— μ_P/μ and LCE volume fraction— μ_P/μ relations with the stiffness ratio (between passive and LCE materials) $\mu_P/\mu = 1$, 2, 4, and 8, respectively. The rise of the stiffness ratio μ_P/μ requires more LCE to achieve an accurate fit. The volume increase is clearly visible in the zoomed-in views of the deformed configurations where the thickness of the LCE layer increases as the stiffness ratio rises.

Using the framework and assuming a nematic-isotropic transition (Q=0), we realize various other target shapes of numbers 3, 6, and 7 as demonstrated in Fig. 5C - E. The corresponding targets are defined by tangentially joining circular arcs and line segments with the radius R, angle θ , and linear length L of each part of the targets given in Fig. 5C - E. All strips show accurate realizations of the target shapes that have drastically different distributions and magnitudes of curvatures along their contour. As expected, the distribution of LCE concentrates in regions with large curvatures, such as the middle region of number 3 and the sharp corner of number 7. By contrast, number 6 features a gradually varying curvature and hence results in a relatively uniform distribution of LCE.

4.2. Programming the planar deformed shape of LCE composite sheet

This subsection focuses on programming the planar deformed shape of 2D sheets made of LCE composites upon temperature rise. Planar spontaneous deformation of LCE can be harnessed for bio-medical applications [12] and planar accusations [71]. The inverse optimization of LCE distributions for 2D sheets to achieve complex target shapes remains a main challenge. Through several numerical examples, we demonstrate that shapes with wide-ranging complexity can be accurately achieved by rectangular-domain LCE composite sheets.

To represent the 2D shape, we uniformly distribute the control points along the perimeter of the undeformed configuration as illustrated in Fig. 6A. Unlike the slender strip structure, the deformation of the 2D sheet will significantly change the local lengths of the perimeter, and hence, we do not apply the constant arc length assumption and use the general curvature-based formulation (16) (excluding ρ).

To maximize the temperature-induced shape-changing capacity, we use an extremely soft elastomer with $\mu_P = 0.001$ MPa as the passive material. Such soft passive elastomers have been produced and can be 3D-printed (see, for example, [72,73]). For the LCE, we include four candidate directors (M = 4) with angles being 0, $\pi/4$, $\pi/2$, and $3\pi/4$. A nematic-isotropic transition (Q = 0) is used to generate maximal actuation.

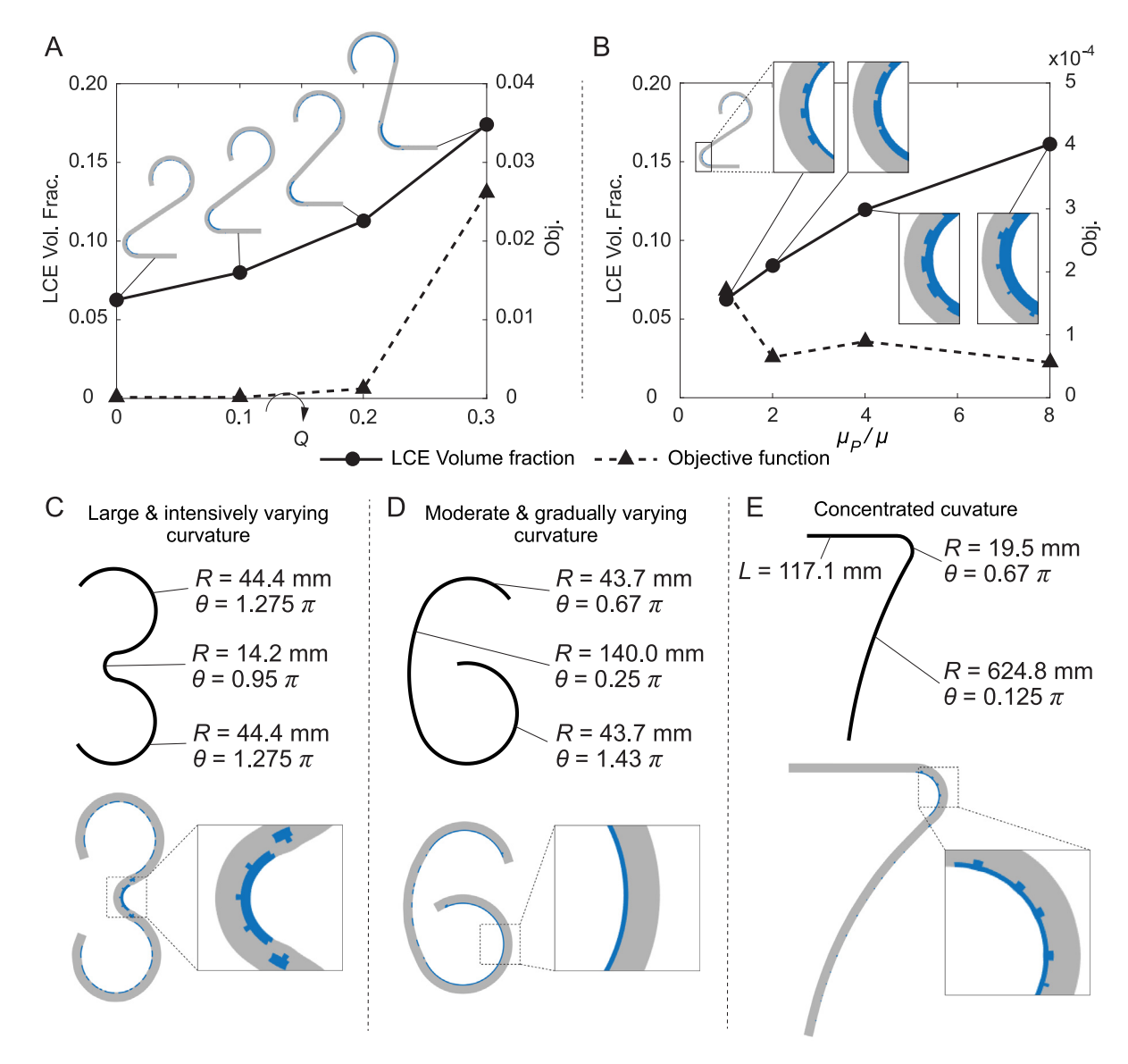


Fig. 5. Parametric study and realization of different target shapes. (A) LCE volume-Q and objective-Q relations; (B) LCE volume- μ_P/μ and objective- μ_P/μ relations; (C) - (E) target shapes and optimized (deformed) design of numbers 3, 6, and 7, respectively.

4.2.1. Elliptical shapes

We first investigate programming a square sheet of LCE composite to deform into a circle and an ellipse with a 1.6 aspect ratio as illustrated in Figs. 6A and B. For the circle, $\kappa^* = -1/R_0$ is a constant function where R_0 is the radius. For the ellipse, κ^* can be obtained by the ellipse equation. The control points and the FE mesh (120 × 120 elements) are shown in Fig. 6A, where a total of 120 control points are used. Other optimization parameters are as follows (for both cases): α_{LCE} is 0.1, and the filter radius is 6. The average computational time of the entire optimization process for this set of examples is approximately 1 h and 30 min.

The optimized designs are shown in Figs. 6C, and their undeformed and current locations of control points are plotted on top of the target shapes scaled by the optimized C value as shown in Fig. 6D. The deformed shapes demonstrate the accurate realization of the circle and ellipse. Both structures possess relatively irregular distributions of LCE while producing a smooth boundary in the deformed configurations even though the undeformed shape has

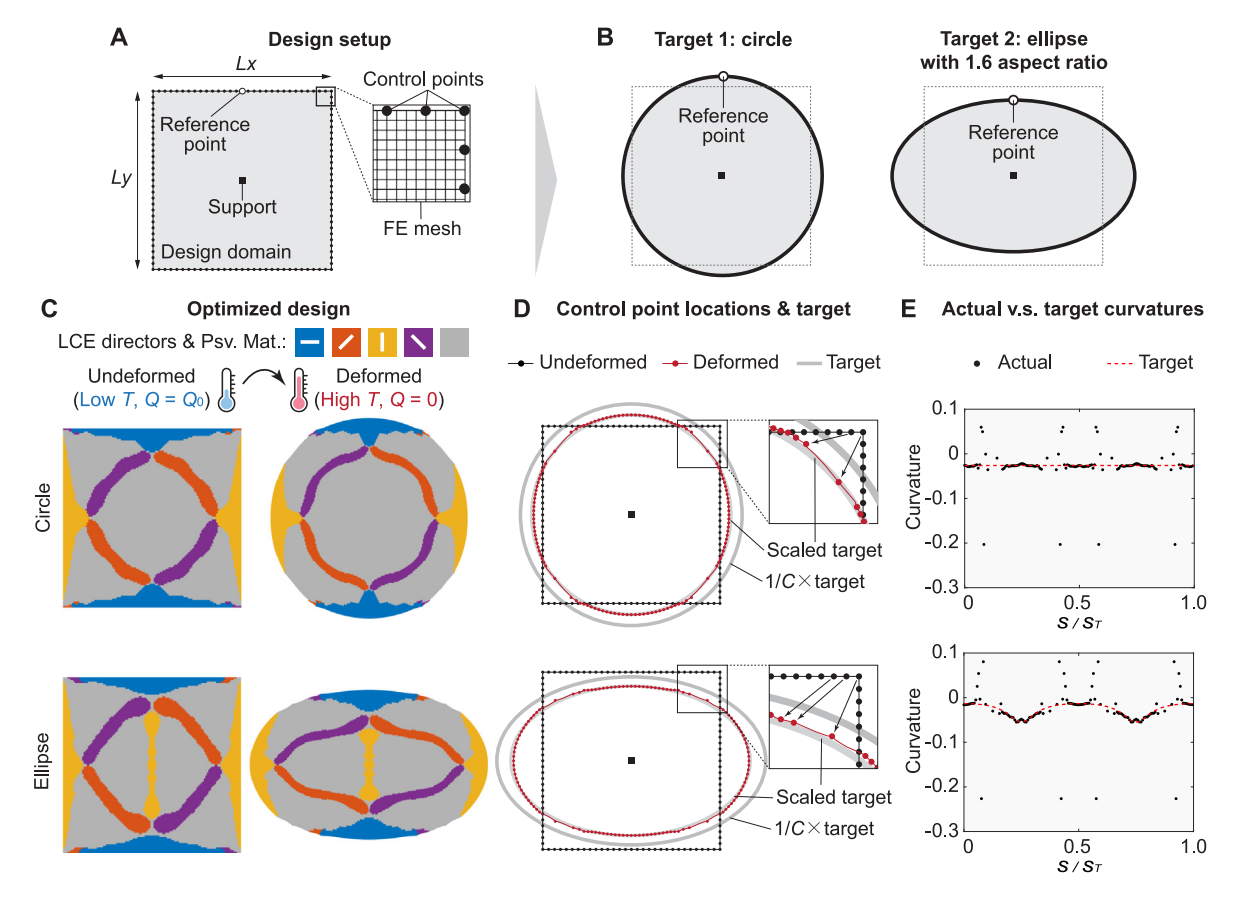


Fig. 6. Inverse optimization of LCE sheet to realize circular and elliptical deformed shapes. (A) Optimization setup: domain, BC, FE mesh, and control points; (B) target shapes of a circle and an ellipse with a 1.6 aspect ratio; (C) optimized LCE designs in undeformed and deformed configurations; (D) control point locations, actual scaled target, and target divided by the optimized C in undeformed and deformed configurations; (E) distribution of actual and target curvatures along the perimeter of the sheet. (For interpretation of the references to color in this figure legend, the reader is referred to the web version of this article.)

four sharp corners. The optimized distribution reveals the mechanism for achieving the target shape. The four sides are occupied by LCEs with directors parallel to the side (the blue and yellow parts) to generate contraction while the four internal members with $\pi/4$ and $3\pi/4$ directors adjust the internal displacement fields. These features are present for both the circle and the ellipse. The ellipse has an extra vertical member at the center with $\pi/2$ director (yellow), which generates vertical contraction and squeezes the sheet into an ellipse. Therefore, although seemingly irregular, the LCE distributions reveal different roles for each of the LCE members. These optimized distributions and sizes are generally difficult to attain by intuition.

As demonstrated in Fig. 6D, the distance among the control points of the current configuration varies significantly along the perimeter, which necessitates the use of current arc lengths to accurately compute curvature. Such large curvature variation is absent in the strip structure. Fig. 6E shows the distribution of the control point's curvatures along the perimeter with their targets scaled by the optimized C (which gives the actual target), demonstrating accurate fitting. A few data points associated with control points near the corners show large shifts from the target, but the impact of such shifts on the overall fitting seems negligible as it is local.

4.2.2. Complex shapes

Using the general formulation (16), we investigate target shapes with more complex geometries, including the shape of a cross, an apple, and the letter "I", as shown in Fig. 7A. For the cross and apple targets, the domain, mesh size, supports, and filter radius are the same as those for the circle and ellipse. For the "I" shape, we use a

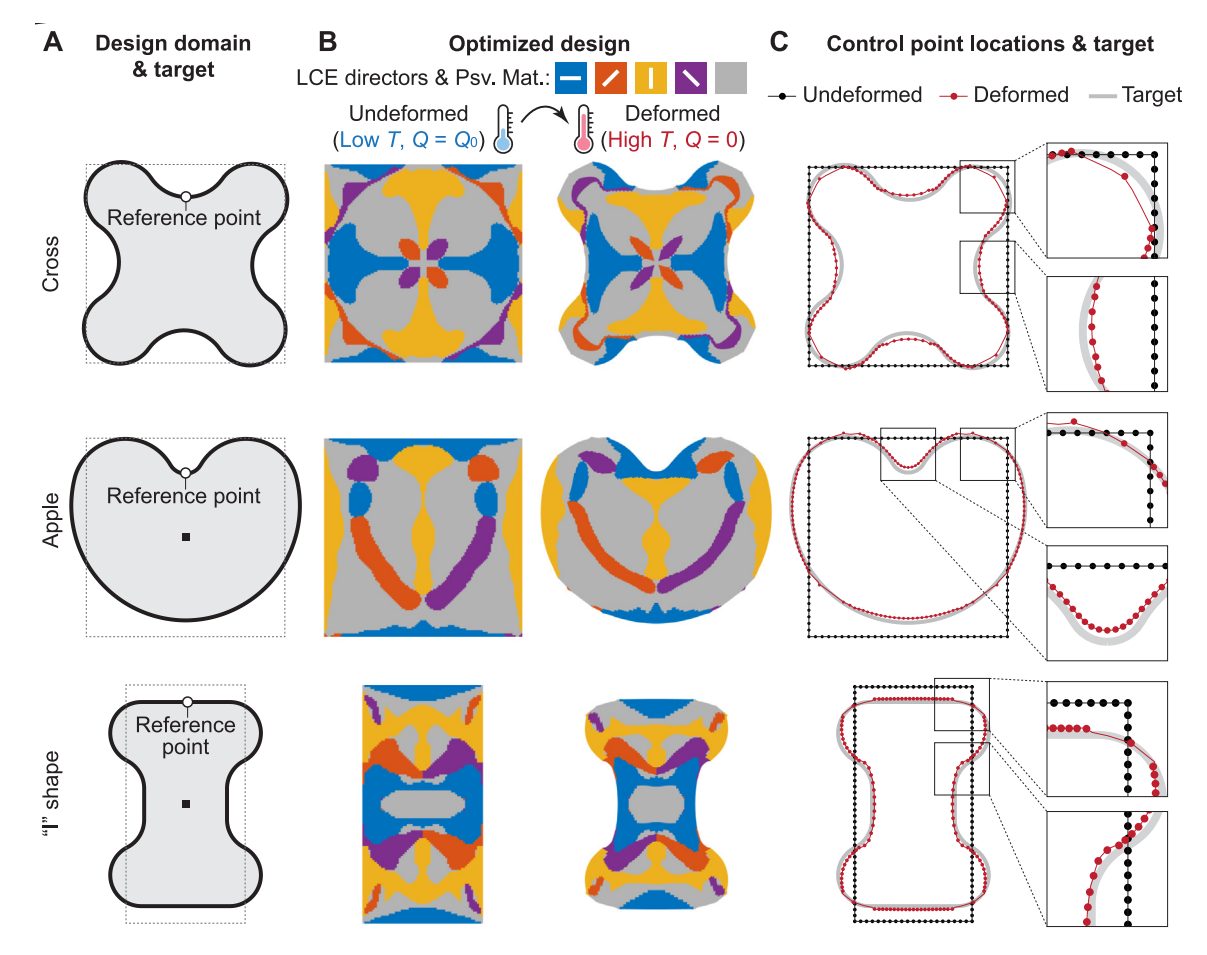


Fig. 7. Inverse optimization of LCE sheet to realize target deformed shapes of a cross, apple, and "I" shape. (A) Domain, BC, and target deformed shapes; (B) optimized designs in undeformed and deformed configurations; (C) control point locations in undeformed and deformed configurations. (For interpretation of the references to color in this figure legend, the reader is referred to the web version of this article.)

rectangular domain with B=60 and H=120, a mesh size 60×120 , and a filter radius of 6.5. The curves of the cross and apple shapes are defined by tangentially joining circular segments with different angles and radii, and the "I" shape additionally includes lines. Note that, unlike the ellipse, these target shapes are non-convex with varying curvatures along the perimeters. Accurate realization of these shapes is highly challenging and beyond the capacity of intuition. The average computational cost of the entire inverse optimization process for apple- and cross-shaped targets is approximately 2 h, and that for the I-shaped target is approximately 1 h.

The optimized designs for the three target shapes are shown in Fig. 7B, and their undeformed and current control point locations are plotted on top of the scaled targets in Fig. 7C. All three optimized LCE composites accurately achieve their targets. For the cross, the blue and yellow members in the middle pull in the center parts of the four sides while the small members near the corners squeeze out the four corners. In general, the optimized geometry of the LCE members is highly irregular and their size varies among different parts. The magnitude and nonlinearity of the members are high as shown in the severely distorted members near the corners. Also, as shown in Fig. 7C, the distance among the originally uniform control points varies significantly in the deformed configuration. Those at the corners were severely stretched while those at the other parts of the boundary are compressed due to LCE contraction. Although severely stretched and compressed, the perimeter of the deformed shape is smooth.

The apple-shaped target is symmetric about the Y-axis only and exhibits large variations of curvature, with the curvatures at the cusp much larger than those at the bottom. As shown in Fig. 7B, the optimized LCE composites accurately achieve the target. The four corners in the undeformed configuration are smoothed. The

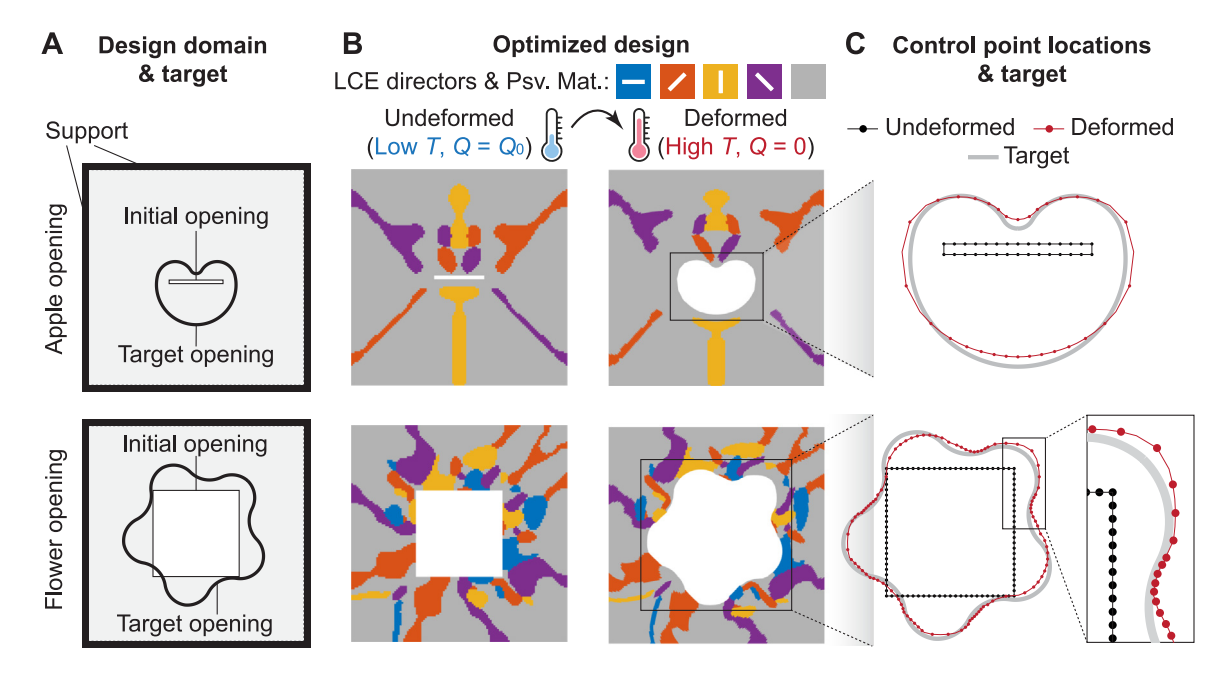


Fig. 8. Inverse optimization of openings inside LCE sheets to realize target deformed shapes. (A) Domain, BC, and target deformed shapes for the openings; (B) optimized designs in undeformed and deformed configurations; (C) control point locations in undeformed and deformed configurations.

accurate realization of the apple shape is enabled by the optimized distribution, geometry, and sizes of the LCE members. The yellow vertical member vertically squeezes the structure. The blue members at the top contract, and, together with the down-pulling of the vertical member, generate the large inward warping representing the cusp. LCE also occupies the other three sides with parallel directors to generate the curved outline. The magnitude of strain and rotation is revealed by the deformed shape and orientation of those small members at the top half.

The I-shaped target has a more sophisticated curvature variation with zero values at the straight parts of the boundary and values with reversed signs at the curved segments. As shown in Fig. 7B, the deformed shape accurately achieves the target. Unlike the previous two designs, the LCE members here are intricately connected and show more complex geometries that seem to form certain mechanisms. The triangular blue LCE members at the top and bottom produce straight segments, and the blue parts in the middle contract horizontally to thin and expand vertically to elongate the middle parts of the "I" shape. The yellow members, together with the purple and orange ones, horizontally expand the top and bottom parts of the "I" shape. Highly irregular and intricately connected, the optimized members jointly produce the target shape difficult to achieve by experience.

4.2.3. Programming shapes for openings

Besides programming the deformed shape of a solid sheet, accurate control of the shape of openings is also valuable for applications such as smart wound closure [12] and thermal management metamaterials [74]. Here, we use the proposed formulation to inversely optimize the deformed shape of openings in a sheet. We consider two setups as illustrated in Fig. 8A. Setup 1 has a thin gap in the middle of the sheet with a target shape of an apple, and Setup 2 has a square opening with a diagonally symmetric flower-shaped target. For both setups, the control points are evenly distributed along the perimeter of the opening. Both domains are fixed at the exterior boundaries and have a size of 120 mm \times 120 mm. The domain is discretized in both directions by 120 finite elements. The filter radius is 4.8 for the first setup and 3.6 for the second. The average computational costs of the entire inverse optimization process for Setup 1 and Setup 2 are approximately 1 h and 30 min and 1 h, respectively.

For the first setup, the giant difference in the geometry, aspect ratio, and, potentially, size between the undeformed gap and the apple-shaped target makes the problem highly challenging. The optimized design is shown in Fig. 8B, which demonstrates the accurate realization of the apple-shaped opening. The five bar-like members attached to the

supports have directors parallel to their overall orientations, which pulls and expands the gap into a much larger opening. The small LCE members at the top produce the large curvature at the top of the opening. While the basic mechanism is clear, the shapes of the members are finely tuned by the optimizer to accurately fit the complex target shape.

The optimized design of the second setup is shown in Fig. 8B, demonstrating the accurate attainment of the flower-shaped target. The distribution of the LCE is highly complex and varies intensively along the boundary of the opening to generate the fluctuating curvature while several members with larger sizes are attached to the support to pull and expand the opening. The complex LCE distribution produces highly nonlinear deformations as demonstrated by the severely distorted LCE members in the deformed configuration. Such non-uniform LCE distributions are beyond the reach of intuition.

The non-uniformity of the control points can be seen in the deformed boundary shown in Fig. 8C. The distribution is dense in the concave regions and loose in the convex parts. As reviewed in the zoomed-in view of Fig. 8C, the difference in the segment lengths can reach over 6 times, which showcases the strength and robustness of the curvature-based formulation (16).

4.3. LCE actuators

In this subsection, we generate LCE actuators that maximize output displacement (and energy) induced by LCE's spontaneous deformation upon temperature change. The large spontaneous deformation makes LCE a strong candidate for thermomechanical actuation, especially for soft structures. Existing ways of actuation that output mechanical work mainly relies on the material-level axial contraction of LCE. However, for more sophisticated boundary conditions, how to optimize the LCE structure to maximize output work remains underexplored. Also, the interplay between LCE and passive material in the context of generating actuation is unclear.

For the LCE actuator, we include the optimization of structural topology through the density design variable ρ in addition to material distribution. Also, we consider passive materials with a much higher stiffness than LCE's. This is in contrast to previous applications where only the material distribution is optimized, and the passive material is soft. As will be demonstrated later, the high stiffness of passive material promotes larger actuation.

The penalization parameters p and p_{ξ} are both set to 3, a conventional value. For the Heaviside parameters β_{ρ} and β_{ξ} , we apply a continuation scheme as the following. Both parameters are initially set to 1, then β_{ρ} starts to increase at the 100th step by a factor of 2 until reaching 64 at the 220th step, and then β_{ξ} starts to increase with the same pattern until reaching 64 at 340th step. The maximum optimization step is set to 360.

The optimization setup of the LCE actuator is shown in Fig. 9A. The size of the rectangular domain is 240 by 60 mm. The domain is fixed on both sides and connected to a spring at the mid-point of the top surface. The spring mimics the stiffness of the external structures being actuated by the LCE structure and measures the actuation power. To exploit symmetry, we use the right half of the domain for the optimization where the original axis of symmetry is constrained laterally by rollers. For passive materials, we investigate a wide range of stiffness with shear modulus ranging between the one of LCE (0.0823 MPa) to 40 MPa. For the spring's stiffness k, we also study a range from 0.05 N/mm to 0.8 N/mm. To remove the potentially excessive concentration of deformation near the spring region, we specify a small passive zone made of 80 MPa passive material as indicated in Fig. 9A. The FE mesh for the half domain is 240 by 120, and the filter radius is 3.6 mm. The average computational cost is approximately 2 h and 30 min.

The optimization objective function for maximizing actuation displacement is:

$$J(\rho, \xi, u(\rho, \xi)) = l \cdot u(\rho, \xi), \tag{18}$$

where the constant vector l extracts the y displacement of the actuated node. Note that the density design variable ρ is included for the optimization of structural topology. Also, we impose a 30% volume fraction constraint for the total (not respective) volume of LCE and passive material. The filter radii for density and material design variables are both 3.6 mm.

We first investigate the setup with $\mu_P = 40$ MPa and k = 0.05 N/mm. The optimized design is shown in Fig. 9B with a maximized actuation displacement of 16.13 mm. Both the stiff passive material and LCE with 0-, 45-, and 135-degree orientations appear, indicating the optimizer's preference for a composite instead of a purely LCE structure. The passive material parts have detailed features such as holes and branches while the LCE parts

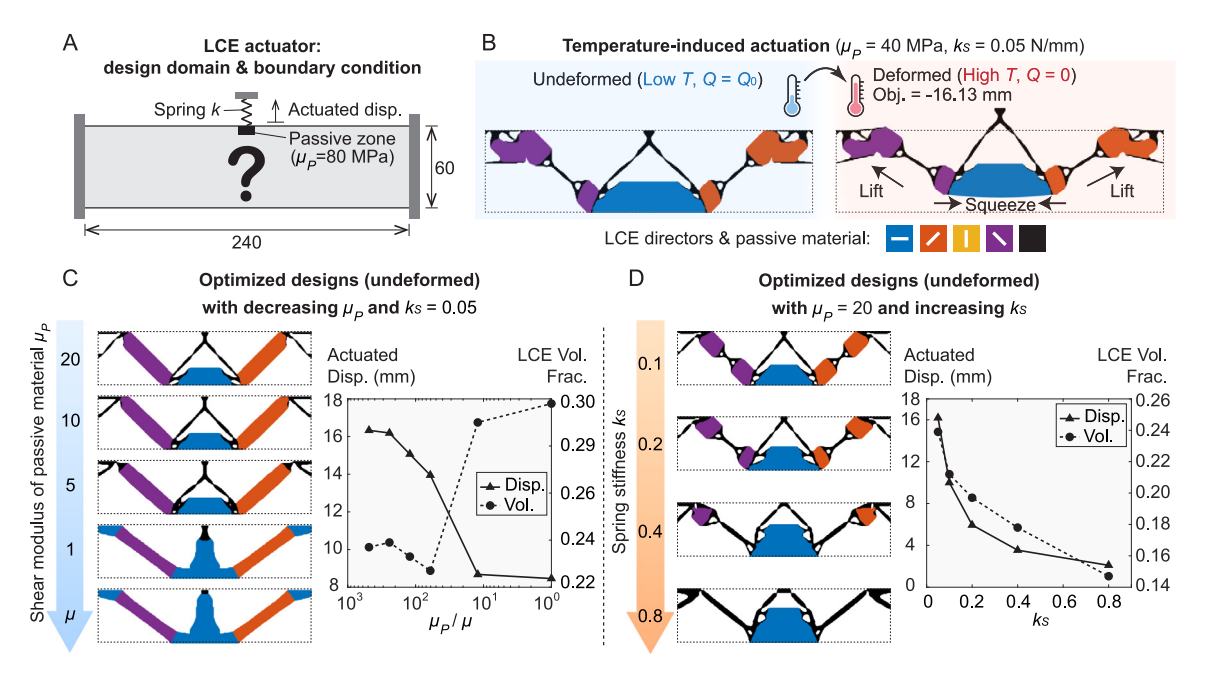


Fig. 9. Topology optimization of LCE actuator with maximized output displacement. (A) Optimization setup: domain and BC; (B) optimized design in undeformed and deformed configuration with $\mu_P = 40$ MPa and k = 0.05 N/mm; (C) optimized designs with decreasing μ_P ; (D) optimized designs with increasing k.

are relatively bulky. The LCE directors largely align with the overall structural orientation. The 0-degree LCE at the bottom and 45- and 135-degree LCE at the left and right regions contract axially to efficiently squeeze and lift the passive slender bar connecting to the spring. The parts with passive materials serve as supports and connectors. At the top-left and top-right corners, the passive material forms a stiff truss and extends toward the center to serve as a stiff support for the LCE actuation. For other regions, the passive material form thin bars to connect different LCE parts. Note that the passive parts are separated instead of integrated as a complete structure for the latter would boost the overall structural stiffness and significantly impedes the actuation. Hence, the appearance and disconnection of passive materials are generally favorable for LCE actuators.

The stiffness of the passive material (relative to that of LCE) considerably impacts the optimized design and the output displacement. This is demonstrated in Fig. 9C, which shows the optimized designs and objective function values with μ_P decreasing from 20 to 0.0820 MPa (μ). The designs with $5 \le \mu_P \le 20$ form integrated LCE parts, and the passive material parts at the right support form triangular trusses that serve as supports. Those with $\mu_P \le 5$ is dominated by LCE with a significantly lower fraction of passive material, which is concentrated near the spring. In terms of output displacement, the decrease of μ_P reduces the output displacement in a nonlinear fashion as demonstrated in Fig. 9C. With large enough μ_P , the displacements seem to converge to a value of approximately 16.1; and when μ_P is close to μ , the output displacement also converges to a smaller value of approximately 8.2, which is about half of the value with high μ_P . The trend that stiffer passive materials increase output displacement is opposite to the observation in the shape-fitting function in Examples 1 and 2 where softer passive materials enable larger deformation. Also decreasing nonlinearly with μ_P is the volume fraction of the passive material, as demonstrated in Fig. 9C. When μ_P is close to μ , the optimizer favors purely LCE structures. It is expected that when μ_P is further decreased to be smaller than μ , passive material will remain absent in the final result.

The spring's stiffness also significantly influences the optimized design and output displacement as demonstrated in Fig. 9D, where the four results are obtained with a spring's stiffness of 0.1, 0.2, 0.4, and 0.8, respectively. As expected, stiffer springs results in lower actuation but in a nonlinear fashion as shown in Fig. 9D. Surprisingly, the increase in the spring's stiffness reduces the total amount of LCE in the final designs as demonstrated in the plot of LCE volume fraction-k relation in Fig. 9D, indicating that less LCE and more passive material are more efficient for actuation with stiff springs. This seems to contradict the intuition that more actuating material should

be favored for higher resistance. Also, as the *k* increases, the volumes of the 45- and 135-degree LCE reduce while the volume of 0-degree LCE increases. This shows that, in generating actuation, the squeezing effect provided by the 0-degree is more efficient than the lifting effect produced by the 45- and 135-degree LCE.

5. Concluding remarks

This study has developed a robust inverse optimization framework for arbitrary shape programming of LCE composites under temperature-induced deformations. The framework is built upon a rigorous LCE model and multimaterial, multiphysics topology optimization with finite deformation. We propose a curvature-based optimization formulation that accurately captures the inherent geometry of the deformed configuration without being restricted by the overall orientation and scale of the structure. This offers a huge search space for optimization and allows for diverse realizations of any target shape. Several numerical examples have demonstrated the capacity and generality of the optimization framework in accurately achieving a wide range of target shapes with different complexities. For the actuation of LCE composites, we found that passive materials with higher stiffness produce larger actuation and that the stiffness of the passive material and spring has significant but seemingly counter-intuitive impacts on the optimized designs. The proposed framework facilitates systematic function-oriented creation of LCE structures, which will benefit applications such as active metamaterials, soft robotics, and environment-aware actuators.

We identify several directions for future research to address the limitations of the current framework. The first limitation relates to the LCE modeling and design setup. The study focuses on the situation of frozen directors, which is realized when LCE is crosslinked at low temperatures, but this may not always be realizable or preferred in some fabrication scenarios. For LCE crosslinked at high temperatures, the frozen director condition may be invalid and should be lifted. Also, we have focused on the two-dimension plane stress setup, which could also be restrictive for practical applications, such as 3D structures. Hence, a valuable direction would be an extension of the inverse design strategy to LCE with free directors and three dimensions. Such an extension would lead to a considerable increase in computational cost because of the curse of dimensionality and the increase in the number of state variables.

The second limitation in the study is the absence of experimental validation, and hence, a vital future direction is to experimentally validate the programmed responses. A major potential challenge is the fabrication of the multimaterial LCE structure with irregular geometries and material distributions. One can use 3D/4D printing, such as Direct Ink Writing, in which ensuring the interfacial bonding of LCE parts with different directors needs investigation, as the print path may be discontinuous near the interface. Another potential challenge relates to the steady and precise control of the temperature. In the lab environment, this can be realized by an oven. However, the uniformity and rate of thermal loading may be challenging to control precisely in practical applications. Fast loading can trigger the viscous effect and alter the deformation path. Hence, a non-steady-state verification of the steady-state programmed behaviors shall be carried out.

Declaration of competing interest

The authors declare that they have no known competing financial interests or personal relationships that could have appeared to influence the work reported in this paper.

Data availability

Data will be made available on request.

Acknowledgments

Authors X.S.Z. and W.L. acknowledge the support from U.S. National Science Foundation (NSF) CAREER Award CMMI-2047692.

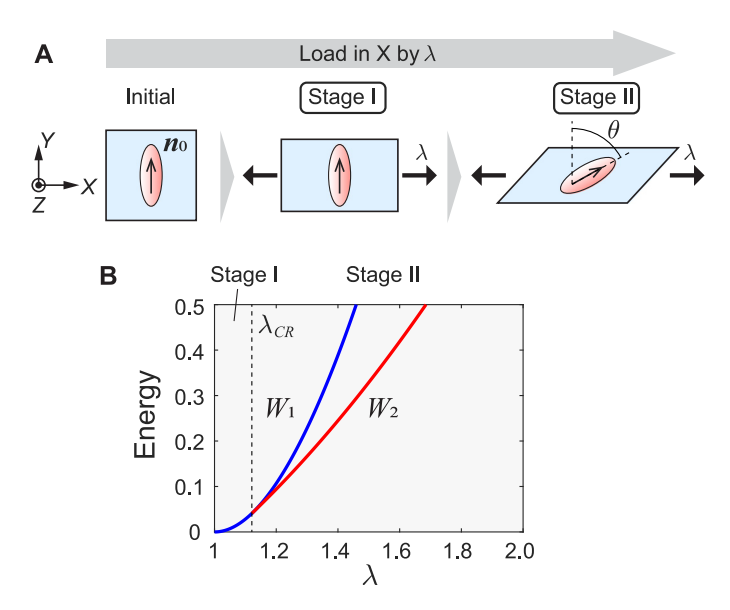


Fig. A.10. Energy of the LCE stretched perpendicular to n_0 . (A) Illustration of the stretch experiment and the two-stage response; (B) stored energies as functions of the applied stretch.

Appendix A. Semi-soft elasticity with frozen director: isothermal stretch of LCE perpendicular to n_0

Here, we analytically investigate the semi-soft elasticity of LCE modeled by the non-ideal frozen-director model (3). For the case where the director can rotate relative to the matrix, the semi-soft response is well-established. Interested readers are referred to [15] for details.

To probe the semi-soft response, we study the isothermal stretch of LCE in the direction perpendicular to n_0 , as indicated in Fig. A.10A. The corresponding deformation gradient is assumed to have the general form:

$$\boldsymbol{F} = \begin{bmatrix} \lambda & \tau & 0 \\ 0 & \eta & 0 \\ 0 & 0 & \frac{1}{\lambda \eta} \end{bmatrix} \tag{A.1}$$

where λ is the applied stretch in the X direction, τ is the unknown shear deformation in XY plane, and η is the unknown stretch in Y direction. The special case of $\tau=0$ and $\eta=1/\sqrt{\lambda}$ is the standard uniaxial deformation for an isotropic (and strongly elliptic) hyperelastic material. Here, however, we assume a more general mode of deformation.

Under the applied λ , the stored-energy density function (4) with $\mu=2$ (to remove the factor of $\mu/2$ for convenience), the above deformation (A.1), isothermal condition $Q=Q_0$, and $\mathbf{n}_0=[0,1,0]$ is a function of τ and η :

$$W(\eta, \tau) = \left(\lambda^2 + \eta^2 + \frac{1}{\lambda^2 \eta^2} + \tau^2\right) - A \frac{\lambda^2 \tau^2}{\eta^2 + \tau^2} - 3 \tag{A.2}$$

where $A := \frac{3}{2}(1 - \frac{1}{1+2Q_0}) - \omega$ is independent of deformation. The τ and η under equilibrium are minimizers of $W(\tau, \eta)$. Applying the gradient condition $\partial W(\tau, \eta)/\partial \tau = 0$ and $\partial W(\tau, \eta)/\partial \eta = 0$ leads to the two equations:

$$\tau \left[1 - A \frac{\lambda^2 \eta^2}{(\eta^2 + \tau^2)^2} \right] = 0$$

$$\eta - \frac{1}{\lambda^2 \eta^3} + A \frac{\lambda^2 \tau^2 \eta}{(\eta^2 + \tau^2)^2} = 0$$
(A.3)

By inspection, $\tau=0$ is a solution to the first equation, with which the second equation yields $\eta=1/\sqrt{\lambda}$. This solution corresponds to the standard uniaxial deformation. In the case of $\tau\neq 0$, for the first equation to have a solution, A needs to be positive, and then we can obtain

$$\tau = \pm \sqrt{A^{\frac{1}{3}} - \frac{1}{\lambda^2} A^{-\frac{1}{3}}}$$

$$\eta = \frac{1}{\lambda} A^{-\frac{1}{6}}$$
(A.4)

with the condition $\lambda \ge \lambda_{cr} := A^{-1/3}$, where λ_{cr} is a critical value of the applied λ . The physically observed solution should correspond to the one with the lower energy. The energy from these two solutions are:

$$W_{1}(\lambda) = \lambda^{2} + \frac{2}{\lambda} - 3$$

$$W_{2}(\lambda) = (1 - A)\lambda^{2} + 3A^{\frac{1}{3}} - 3, \quad \text{with } \lambda > \lambda_{cr}$$
(A.5)

For the purpose of this case study, we use $\omega=0.1$ for convenience. The two corresponding $W-\lambda$ relations are plotted in Fig. A.10B with the dashed line representing $\lambda=\lambda_{cr}$. It can be seen that when $\lambda<\lambda_{cr}$, W_1 is the only valid solution, but when $\lambda\geq\lambda_{cr}$, both solutions exist with W_2 producing the lower energy. This indicates the second solution should be the physically observed solution. This also implies that, as λ surpasses λ_{cr} , there is a deformation mode transition from the first solution to the second, generating the coupled shear deformation and different stretches in Y and Z directions. Essentially, the second mode is the semi-soft mode. This is shown in Fig. 2B which plots the applied stress $dW/d\lambda$ -stretch relation for the two solutions. Clearly, the second mode's stiffness is significantly lower than the first one.

Figs. 2C-E also show the $\eta - \lambda$, $\theta - \lambda$, and $\tau - \lambda$ relations, respectively. When $\lambda < \lambda_{cr}$, shear deformation and director rotation are absent, and the stretch in Y and Z directions are equal. When $\lambda \geq \lambda_{cr}$, shear deformation τ and director rotation θ appear, and the stretches in Y and Z start to diverge. The τ grows rapidly in the beginning and asymptotically approaches the upper bound of $A^{1/6}$ as $\lambda \to \infty$. The rotation θ also increases fast initially and later asymptotically approaches the upper bound of $\pi/2$, which is the direction of the applied stretch.

It should be noted that the existence of the semi-soft elasticity (the second solution) depends on the sign of A. This can be seen from the structure of the first equation of (A.3). When A>0, there exists a λ_{cr} beyond which the semi-soft elasticity dominates. However, when $A\leq 0$, that is, when either Q_0 is small enough (highly disordered) or ω is large enough (highly non-ideal), the standard solution $\tau=0$ and $\eta=1/\sqrt{\lambda}$ is the only solution. This mathematical observation agrees with the physical understanding of LCE. For example, at the isotropic state (high temperature) $Q_0=Q=0$, LCE should behave as a normal isotropic elastomer without soft elasticity. These physical indications, which are direct results of the model's mathematical structure, demonstrate the model's effectiveness in capturing realistic LCE behaviors.

Appendix B. Design regularization techniques and variable for stabilizing computation

For density-based topology optimization, Heaviside projection and filtering are standard techniques to regularize the design space, improve the discreteness of the final designs, and achieve mesh insensitivity [27,66]. This study employs both techniques and applies them to the density and material design variables to obtain the two corresponding projected variables. For the density, the projected variable is the physical variable used to represent the geometry and topology of the structure. For the material variable, the projected variable is intermediate and used for the calculation of the physical material variable through the HSP interpolation as elaborated in 3.1.2. The projected variables are computed through

$$\bar{\rho}_e = \frac{\tanh(\beta_\rho \eta_\rho) + \tanh\left(\beta_\rho \left(\tilde{\rho}_e - \eta_\rho\right)\right)}{\tanh(\beta_\rho \eta_\rho) + \tanh(\beta_\rho (1 - \eta_\rho))} \quad \text{and} \quad \bar{\xi}_e = \frac{\tanh(\beta_\xi \eta_\xi) + \tanh(\beta_\xi (\tilde{\xi}_e - \eta_\xi))}{\tanh(\beta_\xi \eta_\xi) + \tanh(\beta_\xi (1 - \eta_\xi))},$$
(S1.1)

where β_{ρ} and β_{ξ} are parameters that control the discreteness of the projection, η_{ρ} and η_{ξ} are projection thresholds, and $\tilde{\rho}_{e}$ and $\tilde{\xi}_{e}$ are filtered variables computed by

$$\tilde{\rho}_{e} = \frac{\sum_{j \in Ne(R_{\rho})} w\left(\mathbf{x}_{j}\right) v_{j} \rho_{j}}{\sum_{j \in Ne(R_{\rho})} w\left(\mathbf{x}_{j}\right) v_{j}} \quad \text{and} \quad \tilde{\xi}_{e} = \frac{\sum_{j \in Ne(R_{\xi})} w\left(\mathbf{x}_{j}\right) v_{j} \xi_{j}}{\sum_{j \in Ne(R_{\xi})} w\left(\mathbf{x}_{j}\right) v_{j}},$$
(S1.2)

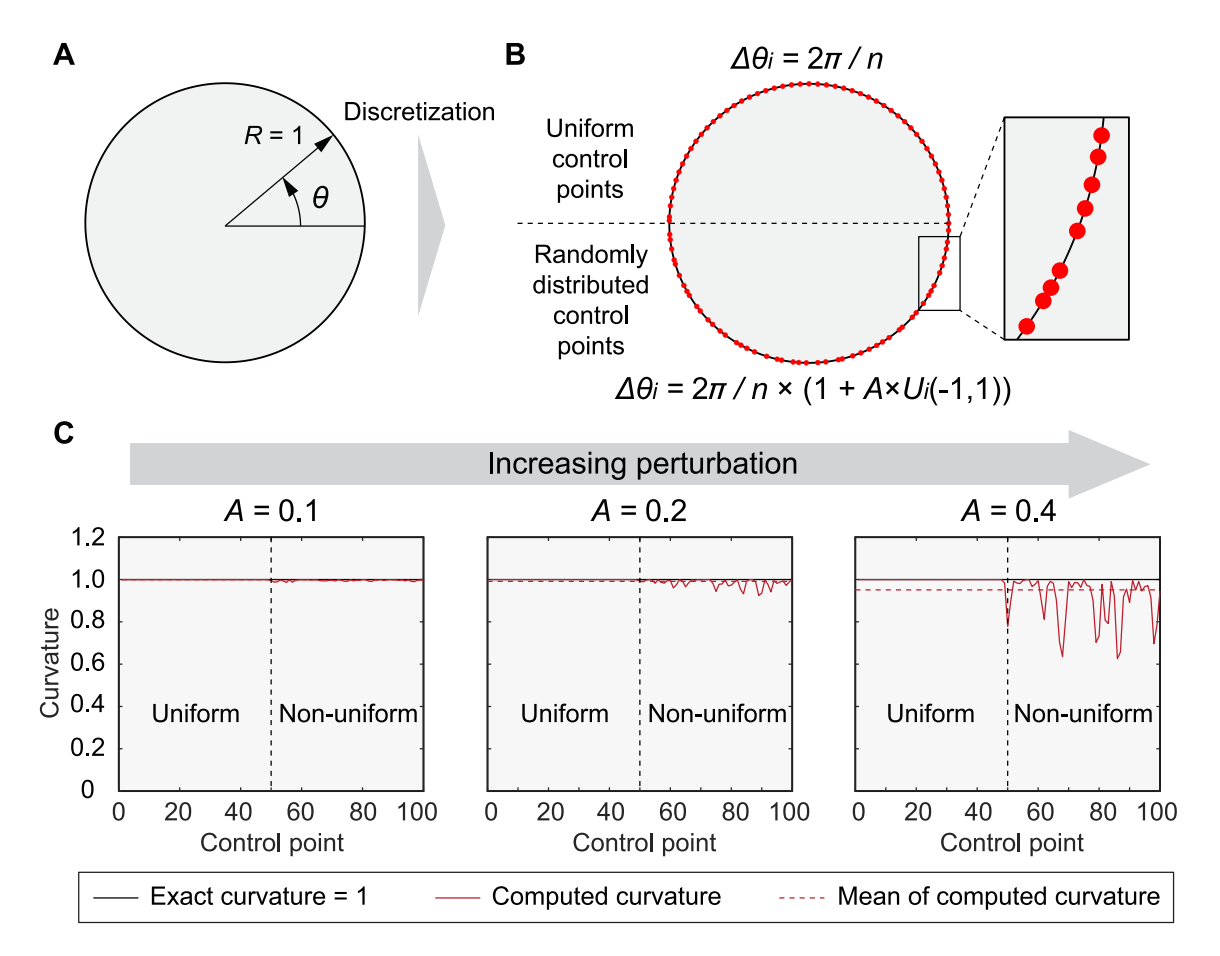


Fig. C.11. Error analysis of the curvature computation (17) based on a unit-radius circle. (A) The unit-radius circle with curvature = 1; (B) the circle discretized by 100 control points: the control points are uniform on the upper half and randomly non-uniform on the lower; (C) distribution of curvatures computed by (17) with different magnitudes of random perturbation.

where x_j is the coordinate of the centroid of element j, v_j is the associated element volume, N_e is the neighborhood of element e defined by a filter radius R, i.e. $N_e(R) = \{j : \|x_j - x_e\| \le R\}$, $w(x_j)$ is the linear weight function defined as $w(x_j) = R - \|x_j - x_e\|$, and R_e are filter radii for e0 and e0, respectively. The filter is essentially a convolution with a linear cone weight field.

The variable γ_e for element e in (9) depends on $\overline{\rho}_e$ through [68]:

$$\gamma_{e}\left(\overline{\rho}_{e}\right) = \frac{\tanh\left(\beta_{\gamma}\rho_{\min}\right) + \tanh\left(\beta_{\gamma}\left(\overline{\rho}_{e}^{p} - \rho_{\min}\right)\right)}{\tanh\left(\beta_{\gamma}\rho_{\min}\right) + \tanh\left(\beta_{\gamma}\left(1 - \rho_{\min}\right)\right)}$$
(B.1)

where $\rho_{\min}=0.01$ is the projection threshold, and $\beta_{\gamma}=500$ ensures a near discrete projection. Hence, γ_e is extremely close to 1 for $\overline{\rho}_e>\rho_{\min}$ and close to 0 for $\overline{\rho}_e<\rho_{\min}$.

Appendix C. Error analysis of the approximated computation of curvature

Here, we analyze the errors of the proposed approximated curvature computation in (17) and then explain the underestimation of curvature observed in Fig. 6. We demonstrate that the error comes from the mismatch between the assumption of uniform control point distribution used in the three-point stencil finite difference in (17) and the actually non-uniform distribution of the control points in the deformed configuration.

We study the curvature computation for a circle with a radius of R=1 as shown in Fig. C.11A. The (exact) curvature for the circle is 1/R=1. We use 100 (discrete) control points distributed on the circle as illustrated in

Fig. C.11B. Importantly, the control points on the upper half of the circle (the first 50 control points) are uniformly distributed, i.e., the distance between adjacent control points is identical; for the lower half of the circle, however, the control points are randomly and non-uniformly distributed. The procedure to generate the non-uniform control points is as follows. First, we equally divide the angle of 2π by n=100, so each angle is $2\pi/n$. The 100 points at this stage are equidistant. Then, we perturb the second half of the angles by a random proportion that follows a uniform distribution. Specifically, $\Delta\theta_i = 2\pi/n(1+A\times U_i(-1,1))$, where A is the magnitude of perturbation, and $U_i(a,b)$ denotes the ith random realization with uniform distribution from -1 to 1. The perturbed angles correspond to perturbed control point locations. As shown in Fig. C.11B, the control points of the lower half circle are generated with A=0.4, which shows significant non-uniformity.

Based on the 100 control points, we compute the curvature distribution using (17). The results with different levels of perturbation for the lower half circle are shown in Fig. C.11C. For all three perturbations, the computed curvature overlaps the exact value for the upper half of the circle where the control points are uniform, indicating (17) gives the accurate calculation of the curvature with equidistant control points. For the lower half of the circle with (random) non-uniform control points, a discrepancy between the computed and exact curvatures appears, and it increases as the perturbation magnitude A grows. For A = 0.1 and 0.2, the errors are mild, but for A = 0.4, the error is noticeable. Note that A should be smaller than 0.5 to avoid self-penetration of the material points, which is impossible for a solid. In other words, A = 0.4 is practically close to the maximum possible level of non-uniformity. Importantly, the computed values are always smaller or equal to the exact value, which indicates an underestimation of curvature (or overestimation of the overall size of the shape). This explains the underestimation of curvature observed in Fig. 6.

We note that, while the non-uniformity used with the three-point stencil formula (17) can introduce error, the error is generally small when the non-uniformity is moderate or the proportion of the non-uniform segment relative to the total perimeter is relatively small. As demonstrated in the numerical examples, the error is likely to manifest itself as an overestimation of the overall size and is unlikely to severely impact the shape.

Appendix D. Post-processing of optimized design: projection to discrete representation

This appendix describes the post-processing of optimized designs to generate discrete designs. The use of smoothed Heaviside projection (described in Appendix B) effectively reduces material mixing but could still sometimes fail to completely remove mixing. Hence, we post-process the optimized designs by projecting the material design variables onto discrete values through least-distance projection. As the regions with non-fully discrete materials are usually very limited and small, the impact of the post-processing on the fitting and objective function is mild. All results shown in the main text are projected designs based on which the performance indices such as fitting errors and volume fraction are evaluated.

References

- [1] E.T. Nilsen, Thermonastic leaf movements: A synthesis of research with Rhododendron, Biol. J. Linnean Soc. 110 (3) (2008) 205–233, http://dx.doi.org/10.1111/j.1095-8339.1992.tb00291.x, arXiv:https://academic.oup.com/botlinnean/article-pdf/110/3/205/14078583/j.1095-8339.1992.tb00291.x.pdf.
- [2] Y.-J. Park, H.-J. Lee, K.-E. Gil, J.Y. Kim, J.-H. Lee, H. Lee, H.-T. Cho, L.D. Vu, I. De Smet, C.-M. Park, Developmental programming of thermonastic leaf movement, Plant Physiol. 180 (2) (2019) 1185–1197, http://dx.doi.org/10.1104/pp.19.00139, arXiv: https://academic.oup.com/plphys/article-pdf/180/2/1185/37271790/plphys_v180_2_1185.pdf.
- [3] N. Peppas, J. Hilt, A. Khademhosseini, R. Langer, Hydrogels in biology and medicine: From molecular principles to bionanotechnology, Adv. Mater. 18 (11) (2006) 1345–1360, http://dx.doi.org/10.1002/adma.200501612, URL https://onlinelibrary.wiley.com/doi/abs/10.1002/adma.200501612, arXiv:https://onlinelibrary.wiley.com/doi/pdf/10.1002/adma.200501612.
- [4] T. Mirfakhrai, J.D. Madden, R.H. Baughman, Polymer artificial muscles, Mater. Today 10 (4) (2007) 30–38, http://dx.doi.org/10.1016/ S1369-7021(07)70048-2, URL https://www.sciencedirect.com/science/article/pii/S1369702107700482.
- [5] T.H. Ware, M.E. McConney, J.J. Wie, V.P. Tondiglia, T.J. White, Voxelated liquid crystal elastomers, Science 347 (6225) (2015) 982–984, http://dx.doi.org/10.1126/science.1261019, URL https://www.science.org/doi/abs/10.1126/science.1261019, arXiv:https://www.science.org/doi/pdf/10.1126/science.1261019.
- [6] A. Kotikian, R.L. Truby, J.W. Boley, T.J. White, J.A. Lewis, 3D printing of liquid crystal elastomeric actuators with spatially programed nematic order, Adv. Mater. 30 (10) (2018) 1706164, http://dx.doi.org/10.1002/adma.201706164, URL https://onlinelibrary.wiley.com/doi/abs/10.1002/adma.201706164, arXiv:https://onlinelibrary.wiley.com/doi/pdf/10.1002/adma.201706164.
- [7] T. Guin, M.J. Settle, B.A. Kowalski, A.D. Auguste, R.V. Beblo, G.W. Reich, T.J. White, Layered liquid crystal elastomer actuators, Nature Commun. 9 (1) (2018) 2531, http://dx.doi.org/10.1038/s41467-018-04911-4.

- [8] Q. He, Z. Wang, Y. Wang, A. Minori, M.T. Tolley, S. Cai, Electrically controlled liquid crystal elastomer–based soft tubular actuator with multimodal actuation, Sci. Adv. 5 (10) (2019) eaax5746, http://dx.doi.org/10.1126/sciadv.aax5746, URL https://www.science.org/doi/abs/10.1126/sciadv.aax5746, arXiv:https://www.science.org/doi/pdf/10.1126/sciadv.aax5746.
- [9] L. Ren, B. Li, Y. He, Z. Song, X. Zhou, Q. Liu, L. Ren, Programming shape-morphing behavior of liquid crystal elastomers via parameter-encoded 4D printing, ACS Appl. Mater. Interfaces 12 (13) (2020) 15562–15572, http://dx.doi.org/10.1021/acsami.0c00027, PMID: 32157863.
- [10] K. Liu, F. Hacker, C. Daraio, Robotic surfaces with reversible, spatiotemporal control for shape morphing and object manipulation, Science Robotics 6 (53) (2021) eabf5116, http://dx.doi.org/10.1126/scirobotics.abf5116, URL https://www.science.org/doi/abs/10.1126/scirobotics.abf5116.
- [11] T.S. Hebner, K. Korner, C.N. Bowman, K. Bhattacharya, T.J. White, Leaping liquid crystal elastomers, Sci. Adv. 9 (3) (2023) eade1320, http://dx.doi.org/10.1126/sciadv.ade1320, URL https://www.science.org/doi/abs/10.1126/sciadv.ade1320, arXiv:https://www.science.org/doi/pdf/10.1126/sciadv.ade1320.
- [12] J. Wu, S. Yao, H. Zhang, W. Man, Z. Bai, F. Zhang, X. Wang, D. Fang, Y. Zhang, Liquid crystal elastomer metamaterials with giant biaxial thermal shrinkage for enhancing skin regeneration, Adv. Mater. 33 (45) (2021) 2106175, http://dx.doi.org/10.1002/adma. 202106175, URL https://onlinelibrary.wiley.com/doi/abs/10.1002/adma.202106175, arXiv:https://onlinelibrary.wiley.com/doi/pdf/10.1002/adma.202106175.
- [13] D.J. Roach, C. Yuan, X. Kuang, V.C.-F. Li, P. Blake, M.L. Romero, I. Hammel, K. Yu, H.J. Qi, Long liquid crystal elastomer fibers with large reversible actuation strains for smart textiles and artificial muscles, ACS Appl. Mater. Interfaces 11 (21) (2019) 19514–19521, http://dx.doi.org/10.1021/acsami.9b04401.
- [14] H. Liu, H. Tian, X. Li, X. Chen, K. Zhang, H. Shi, C. Wang, J. Shao, Shape-programmable, deformation-locking, and self-sensing artificial muscle based on liquid crystal elastomer and low–melting point alloy, Sci. Adv. 8 (20) (2022) eabn5722, http://dx.doi.org/10.1126/sciadv.abn5722, URL https://www.science.org/doi/abs/10.1126/sciadv.abn5722, arXiv:https://www.science.org/doi/pdf/10.1126/sciadv.abn5722.
- [15] M. Warner, E.M. Terentjev, Liquid Crystal Elastomers, Vol. 120, Oxford University Press, 2007.
- [16] M. Chen, M. Gao, L. Bai, H. Zheng, H.J. Qi, K. Zhou, Recent advances in 4D printing of liquid crystal elastomers, Adv. Mater. n/a (n/a) 2209566, http://dx.doi.org/10.1002/adma.202209566, URL https://onlinelibrary.wiley.com/doi/abs/10.1002/adma.202209566, arXiv:https://onlinelibrary.wiley.com/doi/pdf/10.1002/adma.202209566.
- [17] B.A. Kowalski, C. Mostajeran, N.P. Godman, M. Warner, T.J. White, Curvature by design and on demand in liquid crystal elastomers, Phys. Rev. E 97 (2018) 012504, http://dx.doi.org/10.1103/PhysRevE.97.012504, URL https://link.aps.org/doi/10.1103/PhysRevE.97. 012504.
- [18] H. Aharoni, Y. Xia, X. Zhang, R.D. Kamien, S. Yang, Universal inverse design of surfaces with thin nematic elastomer sheets, Proc. Natl. Acad. Sci. 115 (28) (2018) 7206–7211, http://dx.doi.org/10.1073/pnas.1804702115, URL https://www.pnas.org/doi/abs/10.1073/pnas.1804702115, arXiv:https://www.pnas.org/doi/pdf/10.1073/pnas.1804702115.
- [19] S. Xia, L.H. He, Inverse design of axisymmetric shapes in glassy nematic bilayers, J. Appl. Mech. 88 (11) (2021) 111002, http://dx.doi.org/10.1115/1.4051498, arXiv:https://asmedigitalcollection.asme.org/appliedmechanics/article-pdf/88/11/111002/6725898/jam_88_11_111002.pdf.
- [20] D. Castro, H. Aharoni, Shape morphing of planar liquid crystal elastomers, Phys. Rev. Lett. 130 (2023) 178101, http://dx.doi.org/10. 1103/PhysRevLett.130.178101, URL https://link.aps.org/doi/10.1103/PhysRevLett.130.178101.
- [21] D. Duffy, L. Cmok, J.S. Biggins, A. Krishna, C.D. Modes, M.K. Abdelrahman, M. Javed, T.H. Ware, F. Feng, M. Warner, Shape programming lines of concentrated Gaussian curvature, J. Appl. Phys. 129 (22) (2021) 224701, http://dx.doi.org/10.1063/5.0044158, arXiv:https://pubs.aip.org/aip/jap/article-pdf/doi/10.1063/5.0044158/15265105/224701_1_online.pdf.
- [22] F. Feng, D. Duffy, M. Warner, J.S. Biggins, Interfacial metric mechanics: Stitching patterns of shape change in active sheets, Proc. R. Soc. A: Math., Phys. Eng. Sci. 478 (2262) (2022) 20220230, http://dx.doi.org/10.1098/rspa.2022.0230, URL https://royalsocietypublishing.org/doi/pdf/10.1098/rspa.2022.0230.
- [23] T.S. Hebner, R.G. Bowman, D. Duffy, C. Mostajeran, I. Griniasty, I. Cohen, M. Warner, C.N. Bowman, T.J. White, Discontinuous metric programming in liquid crystalline elastomers, ACS Appl. Mater. Interfaces 15 (8) (2023) 11092–11098, http://dx.doi.org/10.1021/acsami.2c21984, PMID: 36791283.
- [24] M. Barnes, R. Verduzco, Direct shape programming of liquid crystal elastomers, Soft Matter 15 (2019) 870–879, http://dx.doi.org/10. 1039/C8SM02174K.
- [25] Y. Zhai, M.T. Tolley, T.N. Ng, Digital programming of liquid crystal elastomers to achieve high-fidelity surface morphing, Appl. Mater. Today 27 (2022) 101501, http://dx.doi.org/10.1016/j.apmt.2022.101501, URL https://www.sciencedirect.com/science/article/pii/S2352940722001366.
- [26] M.P. Bendsøe, N. Kikuchi, Generating optimal topologies in structural design using a homogenization method, Comput. Methods Appl. Mech. Engrg. 71 (2) (1988) 197–224, http://dx.doi.org/10.1016/0045-7825(88)90086-2.
- [27] M.P. Bendsøe, O. Sigmund, Topology Optimization: Theory, Methods and Applications, Springer, Berlin, Heidelberg, 2003, http://dx.doi.org/10.1007/978-3-662-05086-6.
- [28] L.L. Beghini, A. Beghini, N. Katz, W.F. Baker, G.H. Paulino, Connecting architecture and engineering through structural topology optimization, Eng. Struct. 59 (2014) 716–726, http://dx.doi.org/10.1016/j.engstruct.2013.10.032.
- [29] M. Baandrup, O. Sigmund, H. Polk, N. Aage, Closing the gap towards super-long suspension bridges using computational morphogenesis, Nature Commun. 11 (1) (2020) 2735, http://dx.doi.org/10.1038/s41467-020-16599-6.
- [30] N. Aage, E. Andreassen, B.S. Lazarov, O. Sigmund, Giga-voxel computational morphogenesis for structural design, Nature 550 (7674) (2017) 84–86, http://dx.doi.org/10.1038/nature23911.

- [31] A. Sutradhar, G.H. Paulino, M.J. Miller, T.H. Nguyen, Topological optimization for designing patient-specific large craniofacial segmental bone replacements, Proc. Natl. Acad. Sci. 107 (30) (2010) 13222–13227, http://dx.doi.org/10.1073/pnas.1001208107.
- [32] C. Wang, Z. Zhao, M. Zhou, O. Sigmund, X.S. Zhang, A comprehensive review of educational articles on structural and multidisciplinary optimization, Struct. Multidiscip. Optim. 64 (5) (2021) 2827–2880, http://dx.doi.org/10.1007/s00158-021-03050-7.
- [33] Z. Zhao, X.S. Zhang, Topology optimization of hard-magnetic soft materials, J. Mech. Phys. Solids 158 (2022) 104628, http://dx.doi.org/10.1016/j.jmps.2021.104628, URL https://www.sciencedirect.com/science/article/pii/S0022509621002684.
- [34] J. Tian, M. Li, Z. Han, Y. Chen, X.D. Gu, Q. Ge, S. Chen, Conformal topology optimization of multi-material ferromagnetic soft active structures using an extended level set method, Comput. Methods Appl. Mech. Engrg. 389 (2022) 114394, http://dx.doi.org/10.1016/j.cma.2021.114394, URL https://www.sciencedirect.com/science/article/pii/S0045782521006496.
- [35] C. Wang, Z. Zhao, X.S. Zhang, Inverse design of magneto-active metasurfaces and robots: Theory, computation, and experimental validation, Comput. Methods Appl. Mech. Engrg. 413 (2023) 116065, http://dx.doi.org/10.1016/j.cma.2023.116065.
- [36] X. Chen, J. Yvonnet, S. Yao, H. Park, Topology optimization of flexoelectric composites using computational homogenization, Comput. Methods Appl. Mech. Engrg. 381 (2021) 113819, http://dx.doi.org/10.1016/j.cma.2021.113819, URL https://www.sciencedirect.com/science/article/pii/S0045782521001559.
- [37] W. Zhang, X. Yan, Y. Meng, C. Zhang, S.-K. Youn, X. Guo, Flexoelectric nanostructure design using explicit topology optimization, Comput. Methods Appl. Mech. Engrg. 394 (2022) 114943, http://dx.doi.org/10.1016/j.cma.2022.114943, URL https://www.sciencedirect. com/science/article/pii/S0045782522002079.
- [38] H. Chung, O. Amir, H.A. Kim, Level-set topology optimization considering nonlinear thermoelasticity, Comput. Methods Appl. Mech. Engrg. 361 (2020) 112735, http://dx.doi.org/10.1016/j.cma.2019.112735, URL https://www.sciencedirect.com/science/article/pii/S0045782519306255.
- [39] Y. Wang, O. Sigmund, Multi-material topology optimization for maximizing structural stability under thermo-mechanical loading, Comput. Methods Appl. Mech. Engrg. 407 (2023) 115938, http://dx.doi.org/10.1016/j.cma.2023.115938, URL https://www.sciencedirect. com/science/article/pii/S0045782523000610.
- [40] K. Fuchi, T.H. Ware, P.R. Buskohl, G.W. Reich, R.A. Vaia, T.J. White, J.J. Joo, Topology optimization for the design of folding liquid crystal elastomer actuators, Soft Matter 11 (2015) 7288–7295, http://dx.doi.org/10.1039/C5SM01671A, URL http://dx.doi.org/10.1039/C5SM01671A.
- [41] D. Athinarayanarao, R. Prod'hon, D. Chamoret, H.J. Qi, M. Bodaghi, J.-C. André, F. Demoly, Computational design for 4D printing of topology optimized multi-material active composites, npj Comput. Mater. 9 (1) (2023) 1, http://dx.doi.org/10.1038/s41524-022-00962-w.
- [42] A. Akerson, B. Bourdin, K. Bhattacharya, Optimal design of responsive structures, Struct. Multidiscip. Optim. 65 (4) (2022) 111, http://dx.doi.org/10.1007/s00158-022-03200-5.
- [43] M. Warner, K.P. Gelling, T.A. Vilgis, Theory of nematic networks, J. Chem. Phys. 88 (6) (1988) 4008–4013, http://dx.doi.org/10.1063/ 1.453852.
- [44] M. Warner, X.J. Wang, Elasticity and phase behavior of nematic elastomers, Macromolecules 24 (17) (1991) 4932–4941, http://dx.doi.org/10.1021/ma00017a033.
- [45] P. Bladon, E.M. Terentjev, M. Warner, Deformation-induced orientational transitions in liquid crystals elastomer, J. Phys. II France 4 (1) (1994) 75-91.
- [46] S. Conti, A. DeSimone, G. Dolzmann, Soft elastic response of stretched sheets of nematic elastomers: A numerical study, J. Mech. Phys. Solids 50 (7) (2002) 1431–1451, http://dx.doi.org/10.1016/S0022-5096(01)00120-X, URL https://www.sciencedirect.com/science/article/pii/S002250960100120X.
- [47] A. DeSimone, Coarse-grained models of materials with non-convex free-energy: Two case studies, Comput. Methods Appl. Mech. Engrg. 193 (48) (2004) 5129–5141, http://dx.doi.org/10.1016/j.cma.2003.12.064, Advances in Computational Plasticity, URL https://www.sciencedirect.com/science/article/pii/S0045782504002695.
- [48] J. Küupfer, H. Finkelmann, Liquid crystal elastomers: Influence of the orientational distribution of the crosslinks on the phase behaviour and reorientation processes, Macromol. Chem. Phys. 195 (4) (1994) 1353–1367, http://dx.doi.org/10.1002/macp.1994.021950419, URL https://onlinelibrary.wiley.com/doi/abs/10.1002/macp.1994.021950419, arXiv:https://onlinelibrary.wiley.com/doi/pdf/10.1002/macp. 1994.021950419.
- [49] J.S. Biggins, E.M. Terentjev, M. Warner, Semisoft elastic response of nematic elastomers to complex deformations, Phys. Rev. E 78 (2008) 041704, http://dx.doi.org/10.1103/PhysRevE.78.041704, URL https://link.aps.org/doi/10.1103/PhysRevE.78.041704.
- [50] H. Tokumoto, H. Zhou, A. Takebe, K. Kamitani, K. Kojio, A. Takahara, K. Bhattacharya, K. Urayama, Probing the in-plane liquid-like behavior of liquid crystal elastomers, Sci. Adv. 7 (25) (2021) eabe9495, http://dx.doi.org/10.1126/sciadv.abe9495, URL https://www.science.org/doi/abs/10.1126/sciadv.abe9495, arXiv:https://www.science.org/doi/pdf/10.1126/sciadv.abe9495.
- [51] F. Cirak, Q. Long, K. Bhattacharya, M. Warner, Computational analysis of liquid crystalline elastomer membranes: Changing Gaussian curvature without stretch energy, Int. J. Solids Struct. 51 (1) (2014) 144–153, http://dx.doi.org/10.1016/j.ijsolstr.2013.09.019, URL https://www.sciencedirect.com/science/article/pii/S0020768313003740.
- [52] L.A. Mihai, H. Wang, J. Guilleminot, A. Goriely, Nematic liquid crystalline elastomers are aeolotropic materials, Proc. R. Soc. A: Math. Phys. Eng. Sci. 477 (2253) (2021) 20210259, http://dx.doi.org/10.1098/rspa.2021.0259, URL https://royalsocietypublishing.org/doi/abs/10.1098/rspa.2021.0259, arXiv:https://royalsocietypublishing.org/doi/pdf/10.1098/rspa.2021.0259.
- [53] V. Agostiniani, A. DeSimone, Ogden-type energies for nematic elastomers, Int. J. Non-Linear Mech. 47 (2) (2012) 402–412, http://dx.doi.org/10.1016/j.ijnonlinmec.2011.10.001, Nonlinear Continuum Theories, URL https://www.sciencedirect.com/science/article/pii/S0020746211002447.
- [54] S.-Y. Jeon, B. Shen, N.A. Traugutt, Z. Zhu, L. Fang, C.M. Yakacki, T.D. Nguyen, S.H. Kang, Synergistic energy absorption mechanisms of architected liquid crystal elastomers, Adv. Mater. 34 (14) (2022) 2200272, http://dx.doi.org/10.1002/adma.202200272, URL https://onlinelibrary.wiley.com/doi/abs/10.1002/adma.202200272, arXiv:https://onlinelibrary.wiley.com/doi/pdf/10.1002/adma.202200272.

- [55] Z. Wang, A. El Hajj Chehade, S. Govindjee, T.D. Nguyen, A nonlinear viscoelasticity theory for nematic liquid crystal elastomers, J. Mech. Phys. Solids 163 (2022) 104829, http://dx.doi.org/10.1016/j.jmps.2022.104829, URL https://www.sciencedirect.com/science/article/pii/S002250962200045X.
- [56] I. Kundler, H. Finkelmann, Director reorientation via stripe-domains in nematic elastomers: Influence of cross-link density, anisotropy of the network and smectic clusters, Macromol. Chem. Phys. 199 (4) (1998) 677–686, http://dx.doi.org/10.1002/(SICI)1521-3935(19980401) 199:4<677::AID-MACP677>3.0.CO;2-E.
- [57] S.M. Clarke, A. Hotta, A.R. Tajbakhsh, E.M. Terentjev, Effect of crosslinker geometry on equilibrium thermal and mechanical properties of nematic elastomers, Phys. Rev. E 64 (2001) 061702, http://dx.doi.org/10.1103/PhysRevE.64.061702, URL https://link.aps.org/doi/10. 1103/PhysRevE.64.061702.
- [58] S.M. Clarke, A.R. Tajbakhsh, E.M. Terentjev, M. Warner, Anomalous viscoelastic response of nematic elastomers, Phys. Rev. Lett. 86 (2001) 4044–4047, http://dx.doi.org/10.1103/PhysRevLett.86.4044, URL https://link.aps.org/doi/10.1103/PhysRevLett.86.4044.
- [59] G.E. Bauman, J.M. McCracken, T.J. White, Actuation of liquid crystalline elastomers at or below ambient temperature, Angew. Chem. Int. Edition 61 (28) (2022) e202202577, http://dx.doi.org/10.1002/anie.202202577, URL https://onlinelibrary.wiley.com/doi/abs/10.1002/anie.202202577, arXiv:https://onlinelibrary.wiley.com/doi/pdf/10.1002/anie.202202577.
- [60] D.L. Thomsen, P. Keller, J. Naciri, R. Pink, H. Jeon, D. Shenoy, B.R. Ratna, Liquid crystal elastomers with mechanical properties of a muscle, Macromolecules 34 (17) (2001) 5868–5875, http://dx.doi.org/10.1021/ma001639q.
- [61] G. Feio, J.L. Figueirinhas, A.R. Tajbakhsh, E.M. Terentjev, Critical fluctuations and random-anisotropy glass transition in nematic elastomers, Phys. Rev. B 78 (2008) 020201, http://dx.doi.org/10.1103/PhysRevB.78.020201, URL https://link.aps.org/doi/10.1103/ PhysRevB.78.020201.
- [62] N. Cheewaruangroj, E.M. Terentjev, Shape instability on swelling of a stretched nematic elastomer filament, Phys. Rev. E 92 (2015) 042502, http://dx.doi.org/10.1103/PhysRevE.92.042502, URL https://link.aps.org/doi/10.1103/PhysRevE.92.042502.
- [63] O. Zienkiewicz, R. Taylor, D. Fox, The Finite Element Method for Solid and Structural Mechanics, seventh ed., Butterworth-Heinemann, Oxford, 2014, http://dx.doi.org/10.1016/C2009-0-26332-X.
- [64] X.S. Zhang, H. Chi, Z. Zhao, Topology optimization of hyperelastic structures with anisotropic fiber reinforcement under large deformations, Comput. Methods Appl. Mech. Engrg. 378 (2021) 113496, http://dx.doi.org/10.1016/j.cma.2020.113496, URL https://www.sciencedirect.com/science/article/pii/S0045782520306812.
- [65] T.E. Bruns, D.A. Tortorelli, Topology optimization of non-linear elastic structures and compliant mechanisms, Comput. Methods Appl. Mech. Engrg. 190 (26) (2001) 3443–3459, http://dx.doi.org/10.1016/S0045-7825(00)00278-4.
- [66] F. Wang, B.S. Lazarov, O. Sigmund, On projection methods, convergence and robust formulations in topology optimization, Struct. Multidiscip. Optim. 43 (6) (2011) 767–784, http://dx.doi.org/10.1007/s00158-010-0602-y.
- [67] Y. Zhou, T. Nomura, K. Saitou, Multi-component topology and material orientation design of composite structures (MTO-C), Comput. Methods Appl. Mech. Engrg. 342 (2018) 438–457, http://dx.doi.org/10.1016/j.cma.2018.07.039, URL https://www.sciencedirect.com/science/article/pii/S0045782518303839.
- [68] F. Wang, B.S. Lazarov, O. Sigmund, J.S. Jensen, Interpolation scheme for fictitious domain techniques and topology optimization of finite strain elastic problems, Comput. Methods Appl. Mech. Engrg. 276 (2014) 453–472, http://dx.doi.org/10.1016/j.cma.2014.03.021.
- [69] W. Li, F. Wang, O. Sigmund, X.S. Zhang, Design of composite structures with programmable elastic responses under finite deformations, J. Mech. Phys. Solids 151 (2021) 104356, http://dx.doi.org/10.1016/j.jmps.2021.104356, URL https://www.sciencedirect.com/science/article/pii/S0022509621000533.
- [70] K. Svanberg, The method of moving asymptotes—A new method for structural optimization, Internat. J. Numer. Methods Engrg. 24 (2) (1987) 359–373, http://dx.doi.org/10.1002/nme.1620240207.
- [71] M. Barnes, S.M. Sajadi, S. Parekh, M.M. Rahman, P.M. Ajayan, R. Verduzco, Reactive 3D printing of shape-programmable liquid crystal elastomer actuators, ACS Appl. Mater. Interfaces 12 (25) (2020) 28692–28699, http://dx.doi.org/10.1021/acsami.0c07331, PMID: 32484325.
- [72] J. Huang, L. Cao, C.-Y. Xue, Y.-Z. Zhou, Y.-C. Cai, H.-Y. Zhao, Y.-H. Xing, S.-H. Yu, Extremely soft, stretchable, and self-adhesive silicone conductive elastomer composites enabled by a molecular lubricating effect, Nano Lett. 22 (22) (2022) 8966–8974, http://dx.doi.org/10.1021/acs.nanolett.2c03173, PMID: 36374184.
- [73] S. Nian, J. Zhu, H. Zhang, Z. Gong, G. Freychet, M. Zhernenkov, B. Xu, L.-H. Cai, Three-dimensional printable, extremely soft, stretchable, and reversible elastomers from molecular architecture-directed assembly, Chem. Mater. 33 (7) (2021) 2436–2445, http://dx.doi.org/10.1021/acs.chemmater.0c04659.
- [74] J. Kim, S. Im, J.H. Kim, S.M. Kim, S.-M. Lee, J. Lee, J.P. Im, J. Woo, S.E. Moon, Artificial perspiration membrane by programmed deformation of thermoresponsive hydrogels, Adv. Mater. 32 (6) (2020) 1905901, http://dx.doi.org/10.1002/adma.201905901, URL https://onlinelibrary.wiley.com/doi/abs/10.1002/adma.201905901, arXiv:https://onlinelibrary.wiley.com/doi/pdf/10.1002/adma.201905901.